

AD-A076 237

RCA LABS PRINCETON NJ

F/G 13/8

HIGH-ENERGY ION IMPLANTATION FOR MULTIGIGABIT-RATE GAAS INTEGRAL-CIRCUITS(U)

AUG 79 S G LIU , E C DOUGLAS , C P WU

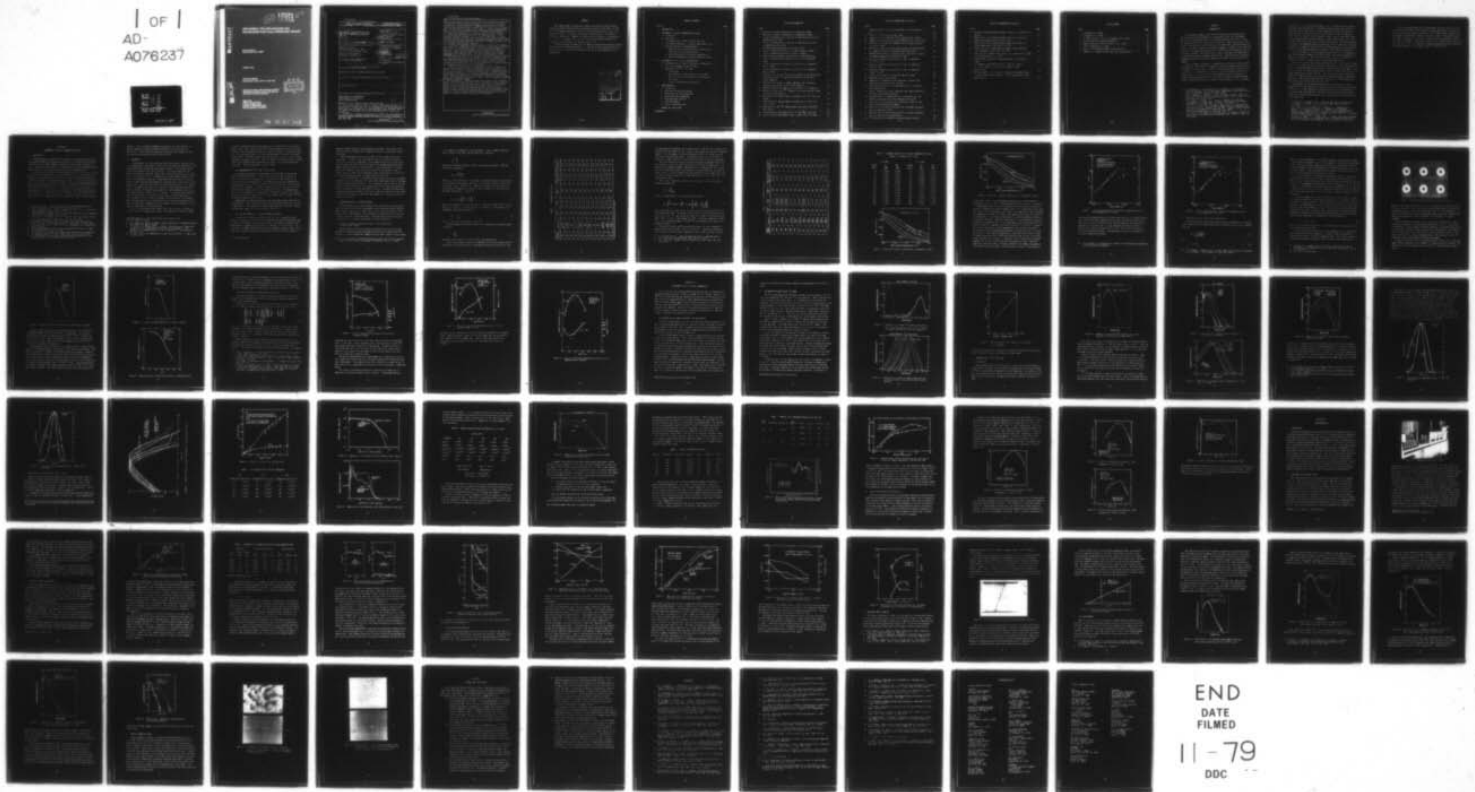
N00014-78-C-0367

UNCLASSIFIED

PRRL-79-CR-37

NL

1 OF 1  
AD-  
A076237



END  
DATE  
FILMED

11-79  
DDC



NATIONAL BUREAU OF STANDARDS  
MICROCOPY RESOLUTION TEST CHART

DA076237

DDC FILE COPY

(12)

LEVEL

4/8

# HIGH-ENERGY ION IMPLANTATION FOR MULTIGIGABIT-RATE GaAs INTEGRATED CIRCUITS

RCA Laboratories  
Princeton, New Jersey 08540

AUGUST 1979

ANNUAL REPORT  
for the period 15 May 1978 to 14 May 1979

Approved for public release; distribution unlimited.  
Reproduction in whole or in part is permitted for  
any purpose of the US Government.

Prepared for  
Office of Naval Research  
Arlington, Virginia 22217  
Contract No. N00014-78-C-0057  
Contract Authority: NR 353-048

DDC  
RECEIVED  
OCT 31 1979  
A

79 10 31 012

⑨ Annual rept. 15 May 78 - 14 May 79

UNCLASSIFIED

SECURITY CLASSIFICATION OF THIS PAGE (When Data Entered)

REPORT DOCUMENTATION PAGE		READ INSTRUCTIONS BEFORE COMPLETING FORM
1. REPORT NUMBER	2. GOVT ACCESSION NO.	3. RECIPIENT'S CATALOG NUMBER
4. TITLE (and Subtitle)		5. TYPE OF REPORT & PERIOD COVERED
⑥ HIGH-ENERGY ION IMPLANTATION FOR MULTIGIGABIT-RATE GaAs INTEGRATED CIRCUIT		Annual Report (5-15-78 to 5-14-79)
7. AUTHOR(s)		6. PERFORMING ORG. REPORT NUMBER
⑩ S. G. Liu, E. C. Douglas, C. P. Wu		⑭ PRRL-79-CR-37
8. PERFORMING ORGANIZATION NAME AND ADDRESS		9. CONTRACT OR GRANT NUMBER(s)
RCA Laboratories Princeton, New Jersey 08850		N00014-78-C-0367
11. CONTROLLING OFFICE NAME AND ADDRESS		10. PROGRAM ELEMENT PROJECT, TASK AREA & WORK UNIT NUMBERS
Office of Naval Research Arlington, Virginia 22217		PE 62762N RF 54-582-001 NR 383-046
14. MONITORING AGENCY NAME & ADDRESS (if different from Controlling Office)		11. REPORT DATE
⑬ F54582 ⑰ RF54582001		August 1979
16. DISTRIBUTION STATEMENT (of this Report)		13. NUMBER OF PAGES
Approved for public release; distribution unlimited.		79
17. DISTRIBUTION STATEMENT (of the abstract entered in Block 20, if different from Report)		15. SECURITY CLASS. (of this report)
18. SUPPLEMENTARY NOTES		Unclassified
19. KEY WORDS (Continue on reverse side if necessary and identify by block number)		16a. DECLASSIFICATION/DOWNGRADING SCHEDULE
High-energy ion implantation Multigigabit-rate GaAs ICs Semi-insulating GaAs		
20. ABSTRACT (Continue on reverse side if necessary and identify by block number)		
<p>The program objectives are: (1) study of high-energy (1 MeV) ion implantation of donors into GaAs for multigigabit-rate integrated-circuit development and (2) annealing of implanted GaAs using high-power lasers to remove lattice damage and activate implanted donors. Results obtained are:</p> <p>(a) We have investigated implantation of <math>^{28}\text{Si}^+</math> into semi-insulating GaAs with implant energies ranging from 40 keV to 1.2 MeV. Secondary</p>		

DD FORM 1 JAN 73 1473

UNCLASSIFIED

SECURITY CLASSIFICATION OF THIS PAGE (When Data Entered)

299 000

JOB



UNCLASSIFIED

SECURITY CLASSIFICATION OF THIS PAGE (When Data Entered)

20

ion-mass spectroscopy (SIMS) profiles show that the projected range increases with implant energy and reaches 1.1  $\mu\text{m}$  at 1.2 MeV. Electron concentration profiles measured on samples implanted at 1 MeV show a peak electron concentration of  $2.2 \times 10^{17}/\text{cm}^3$  for  $1.5 \times 10^{13}$  at./ $\text{cm}^2$  fluence and  $1.0 \times 10^{18}/\text{cm}^3$  for  $1.5 \times 10^{15}$  at./ $\text{cm}^2$  fluence. Van der Pauw measurements on 1-MeV implanted samples show a mobility of about 4000  $\text{cm}^2/\text{V-s}$  and an activation efficiency of  $\sim 74\%$  for  $1.5 \times 10^{13}$  at./ $\text{cm}^2$  fluence.

(b) We have analyzed the profiles and range statistics of  $^{28}\text{Si}$ -implanted GaAs with energies of up to 1.2 MeV using SIMS. A curve-fitting technique, involving the calculation of the first four moments from experimental data, was used to approximate measured profiles. Based on SIMS data, uniformly doped  $^{28}\text{Si}$  profiles  $\sim 1 \mu\text{m}$  deep have been produced in GaAs using multiple implants.

(c) We have investigated laser-annealing of high-dose Si-implanted GaAs using both a high-power Nd:glass laser and a ruby laser. Electrical activation of high-dose, low-energy ( $< 300$  keV) implanted samples are many times higher in laser-annealed samples than for those thermally annealed. Ohmic contacts formed onto laser-annealed samples without alloying have been demonstrated. The surface morphology of laser-annealed samples has been briefly studied by SEM and Nomarski techniques.

(d) Optical absorption in Si-implanted GaAs wafers irradiated with high-power Nd:glass laser pulses has been studied. Measurements show that implantation-enhanced absorption at a given infrared wavelength increases with implant dose. This enhanced absorption is greatly reduced following annealing due to lattice reordering.

(e) Impurity distribution in as-implanted, thermally annealed, and laser-annealed samples has been investigated by SIMS. The amount of impurity redistribution depends on energy and dose of implantation and on the energy density of the annealing laser pulse. Substantial impurity broadening was observed in the high-dose implanted samples irradiated with a high-energy-density ( $\sim 2 \text{ J}/\text{cm}^2$ ) pulse. Anomalous "shoulder broadening" effect was also observed in the SIMS profile of thermally annealed high-dose Si-implanted samples.

(f) Investigation of  $^{28}\text{Si}$  implantations in GaAs at the low-implant energy ( $< 300$  keV) shows that the electron concentration attained has an upper limit at the high-dose region and a lower limit at the low-dose region following thermal annealing. A "cutoff" fluence of about  $2 \times 10^{12}$  at./ $\text{cm}^2$  at 200 keV was observed for most GaAs substrates used. A capless thermal annealing process was used in most of our studies. This anneal is carried out under arsenic overpressure which prevents decomposition of GaAs and results in good surface morphology.

UNCLASSIFIED

SECURITY CLASSIFICATION OF THIS PAGE (When Data Entered)

## PREFACE

This annual report describes the research carried out at the Microwave Technology Center of RCA Laboratories during the period 15 May 1978 to 14 May 1979 in a program sponsored by the Office of Naval Research under Contract No. N00014-78-C-0367. F. Sterzer is the Center's Director and S. Y. Narayan is the Project Supervisor. Members of Technical Staff working on the program are S. G. Liu, E. C. Douglas, and C. P. Wu. The Associate Staff Personnel contributing to the program are F. Kolondra and S. Jain.

The SIMS analyses were made by C. W. Magee of the Materials Characterization Research Section of RCA Laboratories. J. Nering of Fusion Energy Corporation, Princeton, NJ, contributed to setting up their Van de Graaff machine for ion implantation.

Accession for	
DTIC LAM1	
DOW YAD	
Unannounced	
Justification	
By	
Distribution/	
Availability Codes	
Dist.	Avail and/or special
A	

## TABLE OF CONTENTS

Section	Page
I. INTRODUCTION .....	1
II. LOW-ENERGY (<300-keV) IMPLANTATION IN GaAs .....	4
A. Introduction .....	4
B. Substrates .....	5
C. Ion Implantation of $^{28}\text{Si}^+$ and $^{32}\text{S}^+$ into GaAs .....	6
D. Post-Implant Annealing - A Capless Annealing Process .....	6
E. Characterization of Implanted Layers .....	7
1. Mobility, Carrier Concentration, and Activation Efficiency at Various Dose Levels .....	7
2. Depth Distribution of Electron Concentration .....	15
3. Electron Concentration and Hall Mobility Profile .....	20
III. HIGH-ENERGY (UP TO 1.2 MeV) IMPLANTATION .....	24
A. High-Energy Van de Graaff for Heavy Ion Implantation .....	24
B. Calibration Implants Using $^{11}\text{B}^+$ Beam .....	25
C. Implantation of $^{28}\text{Si}^+$ into GaAs .....	27
1. Calibration .....	27
2. The Formation of Flat Profiles of Si in GaAs .....	32
3. Mobility, Carrier Concentration, and Activation Efficiency .....	37
4. Carrier Concentration Distribution .....	40
IV. LASER ANNEALING .....	44
A. Introduction .....	44
B. High-Power Pulsed Laser System .....	44
C. Pulsed Nd:Glass Laser Annealing .....	46
D. Pulsed Ruby-Laser Annealing .....	50
E. Unalloyed Ohmic Contacts .....	54
F. SIMS Measurements .....	56
G. Surface Morphology Study .....	61
V. SUMMARY AND CONCLUSIONS .....	64
REFERENCES .....	66



## LIST OF ILLUSTRATIONS

Figure	Page
1. Mobility vs carrier concentration, S implanted in GaAs .....	12
2. Mobility vs carrier concentration, Si implanted in GaAs .....	13
3. Carrier concentration as a function of implantation dose for S implantation into GaAs .....	14
4. Carrier concentration as a function of implantation dose for Si implantation into GaAs .....	15
5. Photograph showing patterns of Schottky contact .....	17
6. Carrier concentration profile for single-energy Si implant .....	18
7. Carrier concentration profile for dual Si implant .....	19
8. Measured electron density distribution of S-implanted GaAs .....	19
9. Carrier concentration and mobility profile of a S-implanted sample .....	21
10. Carrier concentration and mobility profile of a Si-implanted wafer, 70 keV .....	22
11. Carrier concentration and mobility profile of a Si-implanted wafer, 200 keV .....	23
12. SIMS plots of a 60-keV $^{11}\text{B}$ implant performed on the Laboratories machine and a 1-MeV $^{11}\text{B}$ implant performed on the FEC Van de Graaff implanter .....	26
13. SIMS plots of a group of samples implanted with increasing energies using the FEC Van de Graaff implanter .....	26
14. Measured value of the range $R_p$ for the series of $^{11}\text{B}$ implants ...	27
15. SIMS plot of the first $^{28}\text{Si}^+$ implant into a GaAs substrate using the Van de Graaff machine .....	28
16. SIMS profiles of implants made at energies of 40, 120, 200, and 280 keV .....	29
17. SIMS profiles of implants made at energies of 0.7, 0.8, 0.9, 1.0, 1.2 MeV .....	29
18. SIMS plots of 1-MeV $^{28}\text{Si}$ implants made into GaAs at different dose levels .....	30
19. Curve-fitting to experimental data, 0.7-MeV $^{28}\text{Si}^+$ into GaAs .....	31
20. Curve-fitting to experimental data, 1.18-MeV $^{28}\text{Si}^+$ into GaAs ....	32



# LIST OF ILLUSTRATIONS (Continued)

Figure	Page
21. Composite plots of curves corresponding to the data given in Fig. 17 .....	33
22. Reduction of data to $R_p$ and $\Delta R_p$ values .....	34
23. Comparison of calculated and actual SIMS profiles, log plot .....	35
24. Comparison of calculated and actual SIMS profiles, linear plot .....	35
25. SIMS plots of the multiple-implant profiles formed using different dose levels .....	37
26. Mobility and sheet resistance measured after thermal annealing for samples implanted at different high-energy levels .....	39
27. Measured sheet carrier concentration as a function of Si dose for samples implanted at 200 keV and 1 MeV .....	40
28. Electron concentration distribution, 1-MeV, Si-implanted, $1.5 \times 10^{14}$ at./cm <sup>2</sup> .....	41
29. Electron concentration distribution, 1-MeV, Si-implanted, $5 \times 10^{13}$ at./cm <sup>2</sup> .....	42
30. Electron concentration distribution, 1-MeV, Si-implanted, $1.5 \times 10^{13}$ at./cm <sup>2</sup> .....	42
31. Carrier concentration of a multiple-implanted sample .....	43
32. High-power pulsed laser system .....	45
33. Comparison of thermal and laser annealing; 1.06- $\mu$ m, 25-ns single-pulse (Nd:glass) laser was used .....	47
34. Reflectance measured on an as-implanted wafer (a) and after laser-annealing (b) .....	49
35. Optical transmission from Si-implanted GaAs sample annealed at different laser energy densities .....	50
36. Measured values of transmittance (T), reflectance (R), and enhanced absorption ( $A-A_0$ ) for different dose levels .....	51
37. Sheet electron concentration as a function of dose for ruby-laser and thermal-annealed samples .....	52
38. Mobility ( $\mu$ ), activation efficiency ( $\eta$ ), and sheet resistance ( $\rho_s$ ) as a function of dose .....	53
39. Mobility ( $\mu$ ), activation efficiency ( $\eta$ ), and sheet resistance ( $\rho_s$ ) as a function of energy density .....	54
40. I-V characteristics between two unalloyed ohmic contacts .....	55

# LIST OF ILLUSTRATIONS (Continued)

Figure	Page
41. Resistance between neighboring ohmic contacts as a function of spacing .....	56
42. SIMS profile of a Si-implanted GaAs sample before and after thermal annealing, 200 keV, $5 \times 10^{14}$ at./cm <sup>2</sup> .....	57
43. SIMS profile of a Si-implanted GaAs sample before and after thermal annealing, 70 keV, $3 \times 10^{15}$ at./cm <sup>2</sup> .....	58
44. SIMS profile of a Si-implanted GaAs sample before and after laser annealing, 70 keV, $1 \times 10^{15}$ at./cm <sup>2</sup> .....	59
45. SIMS profiles: unannealed GaAs wafer; laser-annealed at 1 J/cm <sup>2</sup> ; and laser-annealed at 2.3 J/cm <sup>2</sup> .....	60
46. SIMS profiles: unannealed, thermal-annealed, laser-annealed samples .....	61
47. (a) Nomarski interference contrast. Ruby-laser anneal (2.3 J/cm <sup>2</sup> ) sample. (b) SEM of same sample at 20K magnification .....	62
48. SEM photographs. (a) As-implanted sample at 20K magnification. (b) Ruby-laser-annealed sample at 1-J/cm <sup>2</sup> energy density (20K magnification) .....	63

# LIST OF TABLES

Table	Page
1. S Implantation in GaAs .....	9
2. Si Implantation in GaAs .....	11
3. LSS Range Statistics of Si and S Implantation in GaAs .....	12
4. Calculated Multiple Implant Parameters .....	34
5. Implant Conditions for Flat Profile of Si in GaAs .....	36
6. 1-MeV Si Implantation in GaAs .....	38
7. Results of Si-Implanted Wafers at 825 and 970°C .....	39
8. Comparison of Thermal and Nd:Glass Laser Annealing Data .....	48



## SECTION I

### INTRODUCTION

This program is aimed at the study of high-energy ion implantation of donors into GaAs for multigigabit-rate integrated-circuit (IC) development, and the use of high-power lasers for annealing implanted GaAs layers. GaAs ICs require the selective definition of n-layers in semi-insulating (SI) GaAs for the fabrication of active devices such as TELDs, FETs, and Schottky-barrier diodes. In order to fabricate such device elements, a capability for realizing n-layers with doping ranging from  $10^{16}$  to  $5 \times 10^{18} \text{ cm}^{-3}$  and thicknesses from 1 to  $0.15 \text{ }\mu\text{m}$  is required. This implies that we must investigate both implantation of donors with energies ranging from about 100 to 2000 keV and the subsequent annealing process to activate the implants and remove the associated lattice damage.

One of the major problems of ion implantation into GaAs is that the material begins to dissociate at the commonly used anneal temperatures which are in the 800 to 1000°C range. In order to prevent problems associated with dissociation, it is common practice either to use an encapsulant such as  $\text{SiO}_2$ ,  $\text{Si}_3\text{N}_4$ , AlN, etc. or to use a controlled atmosphere with As overpressure. Recent research has shown that it is possible to anneal post-implant damage using a narrow single pulse (or pulses) of laser radiation [1-5], a scanning

1. E. I. Shtyrkov, I. B. Khaibullin, M. M. Zaripov, M. F. Galyatudinov, and R. M. Bayazitov, "Local Annealing of Implantation Doped Semiconductor Layers," *Sov. Phys. Semicond.* 9, 1309 (1976).
2. S. U. Compisano, I. Catalano, G. Foti, E. Rimini, F. Eisen, and M. A. Nicolet, "Laser Reordering of Implanted Amorphous Layers in GaAs," *Solid State Electron.* 21, 485 (1978).
3. R. T. Young, C. W. White, G. J. Clark, J. Narayan, W. H. Christie, M. Murakami, P. W. King, and S. D. Kärner, "Laser Annealing of Boron-Implanted Silicon," *Appl. Phys. Lett.* 32, 139 (1978).
4. S. G. Liu, C. P. Wu, and C. W. Magee, "Annealing of Ion-Implanted GaAs with Nd:Glass Laser," presented at the Symp. on Laser-Solid Interaction and Laser Processing held in Boston, MA. Nov. 28-Dec. 1, 1978. AIP Conference Proceedings No. 50, p. 603, New York, 1979.
5. B. J. Sealy, M. H. Badawi, S. S. Kular, and K. G. Stephens, "Electrical Properties of Laser-Annealed Donor-Implanted GaAs," *Electron. Lett.* 14, 720, (1978).



cw laser [6], or a scanning pulsed laser [7,8]. Very high carrier concentrations have been obtained [4,5] in high-dose implanted GaAs after anneal by high-power pulsed laser beams. We have measured activation efficiencies in laser-annealed Si-implanted GaAs that are more than an order of magnitude higher than for samples annealed thermally. Ohmic contacts have been formed on laser-annealed GaAs surfaces without alloying. These results will be described in Section IV, which also includes the following: the optical absorption study in Si-implanted GaAs before and after laser irradiation, the depth distribution of impurity concentration with SIMS measurements, and preliminary studies on the surface morphology of thermal or laser annealed GaAs wafers.

Until the inception of this program, the major effort on ion implantation into GaAs has been at energies less than 500 keV. Preliminary experiments on implants at energies of 1 MeV and above had shown that it is difficult to anneal out the lattice damage caused by high-energy implantation.

During this program, high-energy implantation of Si into SI GaAs at energy levels up to 1.2 MeV has been successfully demonstrated. A projected range of up to 1.1  $\mu\text{m}$  has been measured by secondary ion-mass spectroscopy (SIMS). Electrical activation following thermal anneal equal to or better than that for low-energy implantation has been obtained. Electron density profiles have been measured on 1- $\mu\text{m}$ -thick GaAs layers produced by multiple-energy Si-implantation and also on 1-MeV single-energy-implanted GaAs layers on SI GaAs substrates. These results will be described in Section III.

The implantation and annealing process and the results on Si- and S-implantation into GaAs substrates at energy levels below 300 keV are presented in Section II. A post-implantation annealing process without encapsulation on the wafer has been developed. The anneal is carried out under an arsenic overpressure which prevents decomposition of GaAs and results in an excellent surface morphology.

6. A. Gat and J. F. Gibbons, "A Laser-Scanning Apparatus for Annealing of Ion-Implantation Damage in Semiconductors," *Appl. Phys. Lett.* **32**, 142 (1978).
7. W. L. Brown, J. A. Gdovchenko, K. A. Jackson, L. C. Kimerling, H. J. Leamy, G. L. Miller, J. M. Poate, J. W. Rodgers, G. A. Rozgonyi, T. T. Sheng, T. N. C. Venkatesan, and G. K. Celler, "Laser-Annealing of Ion-Implanted Semiconductors," *Proc. on Rapid Solidification Proc. - Principles and Technologies*, Reston, VA, Nov. 1977.
8. R. Tsu, J. E. Baglin, G. J. Lasher, and J. C. Tsang, "Laser-Induced Damage and Recrystallization of Ion-Implanted GaAs by Frequency-Doubled Nd:Yag Laser," *AIP Conference Proceedings No. 50*, p. 623, 1979 (c.f. Ref. 4).

Van der Pauw measurements and C-V measurements have been used for evaluation of the electrically active n-layers following implantation and annealing. A novel Schottky diode pattern designed for the C-V measurement eliminates the requirement of making ohmic contacts to the GaAs surface. This method simplifies sample preparation for the electron density profile measurement using automatic profile equipment. The mobility, sheet carrier concentration, and activation efficiency of Si- or S-implanted, thermal-annealed GaAs have been measured with implant fluences in the range of  $2 \times 10^{12}$  to  $5 \times 10^{15}$  at./cm<sup>2</sup>.

## SECTION II

### LOW-ENERGY (<300-keV) IMPLANTATION IN GaAs

#### A. INTRODUCTION

Ion implantation in GaAs has been a subject of considerable interest in recent years because of its potential application in the fabrication of semiconductor devices: FETs, IMPATTs, Gunn devices, laser diodes, and logic circuits. This section describes the ion implantation of sulfur and silicon into GaAs substrates, and the annealing process following implantation.

To produce an n-type layer on GaAs, implantation of S, Se, Te, Si, Sn, and Ge have been used and have been reported previously [9-11]. Following ion implantation, an annealing step is essential to anneal out the lattice defects caused by the impact of high-energy impurity atoms. To prevent dissociation of GaAs at the surface of the wafer, the sample is usually encapsulated during the high-temperature annealing. Various dielectric materials such as  $\text{SiO}_2$  [12],  $\text{Si}_3\text{N}_4$  [13],  $\text{Al}_2\text{O}_3$  [14], AlN [15], the combination of  $\text{SiO}_2$  and  $\text{Si}_3\text{N}_4$  [16], or aluminum metal [17], have been used as encapsulant. The annealing temperature varies from 800 to 1100°C with dielectric encapsulation, and 700°C with Al encapsulation [17]. Annealing without encapsulation either in vacuum, sealed

9. F. H. Eisen et al., "Sulfur, Selenium, and Tellurium Implantation in GaAs," Inst. Phys. Conf. Series No. 28, p. 64, 1976.
10. R. K. Surridge and B. J. Sealy, "A Comparison of Sn-, Ge-, Se- and Te-ion implanted GaAs," J. Phys. D. 10, 911 (1977).
11. J. K. Kung, R. M. Melbon, and D. H. Lee, "GaAs FETs with Silicon Implanted Channels," Electron. Lett. 13, 187 (1977).
12. A. G. Foyt, J. P. Donnelly, and W. T. Lindley, "Efficient Doping of GaAs by  $\text{Se}^+$  Ion Implantation," Appl. Phys. Lett. 14, 372 (1969).
13. B. M. Welch, F. H. Eisen, and J. A. Higgins, "Gallium Arsenide Field-Effect-Transistors by Ion Implantation," J. Appl. Phys. 45, 3685 (1974).
14. W. K. Chu et al., Proc. 3rd Int. Conf. on Ion Implantation, (Plenum Press, New York, 1973).
15. R. D. Pashley and B. M. Welch, "Tellurium-Implanted  $\text{N}^+$  Layers in GaAs," Solid State Electron. 18, 977 (1975).
16. A. Lidow and J. F. Gibbons, "A Double-Layered Encapsulant for Annealing Ion-Implanted GaAs Up to 1100°C," Appl. Phys. Lett. 31, 158 (1977).
17. B. J. Sealy and R. K. Surridge, "A New Thin Film Encapsulant for Ion-Implanted GaAs," Thin Solid Films 26, L19 (1974).



ampoule, or in a controlled atmosphere [18,19] has also been reported. A capless annealing technique different from these will be described in Section II.C. A more advanced annealing technique using a high-power laser has received considerable attention recently [1-8].

## B. SUBSTRATES

Chromium-doped, SI (100)-orientated GaAs substrates were used mostly for our ion-implantation experiments. Studies were also made for implantation into vapor-phase grown, high-resistivity epitaxial layers.\* Semi-insulating substrates were obtained from various sources: Laser Diode, (Metuchen, NJ), Morgan (Garland, TX), Sumitomo (Osaka, Japan), Mitsubishi-Monsato, and Crystal Specialties (Monrovia, CA). Ion-implantation results depend strongly on the quality of the substrate material. Some substrates may convert to either p-type or n-type following high-temperature annealing even in the absence of implanted ions. Substrate qualification is therefore desirable prior to implantation. A normal qualification test consists of implanting the sample with argon or krypton, then annealing the sample at a given temperature and duration (typically 800 to 950°C, for 15 to 30 min). A qualified semi-insulating substrate should show no conversion or activation following annealing. A less stringent test is to anneal the sample alone without prior ion bombardment. Residual impurities in the substrate were reported responsible for the conversion mechanism. Manganese [20], for example, has been reported to be an impurity responsible for the p-conversion.

Before ion implantation the SI substrates require careful cleaning and etching to produce a damage-free surface. The wafers were cleaned in organic

\*VPE layer grown by S. Jolly, RCA Laboratories, Princeton, NJ,  
Contract N00014-77-C-0542

18. A. A. Immoralica and F. H. Eisen, "Capless Annealing of Ion-Implanted GaAs," *App. Phys. Lett.* **29**, 94 (1976).
19. D. H. Lee, R. M. Malbon, and J. M. Whelan, "Characteristics of Implanted N-type Profiles in GaAs Annealed in a Controlled Atmosphere," *Ion-Implantation in Semiconductors*, Ed. by F. Chernow et al. (Plenum Press, New York, 1976).
20. R. Zucca, "Electrical Compensation in Semi-Insulating GaAs," *J. Appl. Phys.* **48**, 1987 (1977).



solvents followed by DI-water rinsing and a 5- to 10-min etch in a solution of  $4\text{H}_2\text{SO}_4:1\text{H}_2\text{O}_2:1\text{H}_2\text{O}$ . The solutions were freshly mixed and cooled to room temperature. After etching the wafers were rinsed in DI-water ( $>14\text{ Mohm}$ ) and spun dry. The etching was done in a tilted rotating beaker to provide a uniformly etched surface. The layer removed was approximately 3 to 6  $\mu\text{m}$ . In cases where implantation through a dielectric layer is required, the wafer surface is either coated with a chemical-vapor-deposited  $\text{SiO}_2$  layer or a reactively sputtered  $\text{Si}_3\text{N}_4$  layer. The layer thickness is 500 to 700  $\text{\AA}$ .

#### C. ION IMPLANTATION OF $^{28}\text{Si}^+$ AND $^{32}\text{S}^+$ INTO GaAs

Low-energy ion-implantation experiments were performed in the 300-keV machine at RCA Laboratories. Silane ( $\text{SiH}_4$ ) was used as the source gas in the rf ion source for Si implantation. Solid sulfur or  $\text{H}_2\text{S}$  in the rf ion source was used for S implantation. The beam current during Si implantation is typically 0.1  $\mu\text{A}$  for low-dose ( $10^{12}$  to  $10^{13}\text{ cm}^{-2}$ ) and up to 10  $\mu\text{A}$  for high-dose ( $10^{15}\text{ cm}^{-2}$ ) implants. A typical implantation at 200 keV with a dose of  $1 \times 10^{14}/\text{cm}^2$  and a beam current of 10  $\mu\text{A}$  takes about 1 min. The maximum beam current level attainable for S implantation at 200 keV is about 5  $\mu\text{A}$ . Implantation was studied with fluences in the range between  $1 \times 10^{12}$  and  $3 \times 10^{15}\text{ at./cm}^2$ , and energies between 50 and 250 keV.

High-energy ( $>500\text{ keV}$ ) implantations were performed using a 3-MeV Van de Graaff machine. Silane ( $\text{SiH}_4$ ) was used as the source gas in the ion source for Si implantation. The implantation energy ranged from 500 to 1200 keV. Details on high-energy implant will be described in Section III.

#### D. POST-IMPLANT ANNEALING - A CAPLESS ANNEALING PROCESS

We developed a capless annealing process [21] for ion-implanted GaAs wafers. The anneal is carried out at a temperature between 800 and 850°C under an arsenic overpressure in an open quartz tube. The arsenic overpressure was maintained by a constant flow of 75 ml of 7.5%  $\text{AsH}_3$  in 2 liters of  $\text{H}_2$ . The introduction of  $\text{AsH}_3$  differs from a previously reported capless process [18,19]. Under this condition the arsenic overpressure at 850°C is over two orders of

21. To be published.

magnitude higher than the equilibrium partial pressure. The arsenic overpressure prevents decomposition of GaAs and results in an excellent surface morphology.

Anneal experiments were also performed on wafers encapsulated with a  $\text{Si}_3\text{N}_4$  layer. A typical layer thickness was 2000 to 3000 Å, and annealing was carried out in a  $\text{N}_2$  atmosphere. Both plasma-deposited  $\text{Si}_3\text{N}_4$  layers and reactive-sputtered  $\text{Si}_3\text{N}_4$  layers were tested. The plasma  $\text{Si}_3\text{N}_4$  encapsulated samples showed blisters following an 850°C, 30-min annealing in a  $\text{N}_2$  atmosphere, while samples encapsulated with sputtered  $\text{Si}_3\text{N}_4$  showed no sign of blistering up to 1000°C and the implanted layers were properly activated with good surface morphology under the same annealing conditions.

The laser annealing of ion-implanted semiconductors has been investigated recently [1-8] as an alternative for the thermal annealing of lattice disorders created by high-energy irradiation. This technique is attractive for its simplicity, potential capability of annealing small local areas, and annealing without encapsulation of the semiconductor surface. During this program both a high-power Q-switched Nd:glass laser and a ruby laser were used in the study of lattice reordering in Si-implanted GaAs samples [4]. Details will be described in Section IV.

#### E. CHARACTERIZATION OF IMPLANTED LAYERS

Following implantation and annealing, the electrically active layer was characterized by van der Pauw measurements, which determine the Hall mobility, sheet carrier concentration, conductivity, and activation efficiency of the n-layer; and C-V measurements, which determine the depth profile of the electrically activated ion-implanted layer. Characteristics of the low-energy (<300 keV) Si- or S-implanted GaAs wafers are described below.

##### 1. Mobility, Carrier Concentration, and Activation Efficiency at Various Dose Levels

The Hall mobility and sheet carrier concentration of the electrically activated ion-implanted layer were measured by the van der Pauw method [22]. A square or a clover-shaped mesa sample with four ohmic contacts at the corners

22. L. J. van der Pauw, "A Method of Measuring Specific Resistivity and Hall Effect of Doses of Arbitrary Shape," Philips Res. Rep. 13, 1 (1958).

of the sample was prepared for the measurement. Typical sample dimensions were 7x7 mm to 9.5x9.5 mm. The Hall mobility is given by

$$\mu_H = \frac{R_S}{\rho_s} \quad (1)$$

where  $R_S$  is the Hall coefficient and  $\rho_s$  is the sheet resistance. The Hall coefficient is given by

$$R_S = 10^8 \frac{\Delta V_{24}}{B I_{13}} \quad (2)$$

where  $I_{13}$  is the current,  $B$  is the magnetic flux density applied perpendicular to the surface of the sample, and  $\Delta V_{24}$  is the voltage change with and without the magnetic field. The subscript numbers correspond to the four ohmic contacts, which are numbered in sequence, either clockwise or counterclockwise. The sheet resistance  $\rho_s$  is given by

$$\rho_s = \frac{\pi}{2 \ln 2} \left( \frac{V_{34}}{I_{12}} + \frac{V_{23}}{I_{41}} \right) \cdot F \quad (3)$$

where  $F$  is a geometrical correction factor. A relation between  $F$  and the ratio  $(V_{34}/I_{12})$  to  $(V_{23}/I_{41})$  is given in ref. 22. From Eq. (1), the sheet carrier concentration  $N_S$  can be expressed as

$$N_S = \frac{1}{q R_S} \quad (4)$$

where  $q$  is the electronic charge ( $1.6 \times 10^{-19} \text{C}$ ).

The percentage activation efficiency for an implanted and annealed sample is given by

$$\eta = \frac{N_S}{N_S^*} \quad (5)$$

where  $N_S^*$  is the fluence (in  $\text{at./cm}^2$ ) used in the implantation.

Table 1 lists typical results on S implantation into semi-insulating substrates and into substrates with a vapor-phase epitaxially grown buffer layer.



TABLE 1. S IMPLANTATION IN GaAs

SAMPLE NUMBER	SUBSTRATE	ENERGY (keV)	DOSE (cm <sup>-2</sup> )	MOBILITY (cm <sup>2</sup> /V-s)	APPROX. CARRIER CONC. (cm <sup>-3</sup> )	ACTIVATION EFF (%)
62B	Si (MM-G103)	200	4.0 x 10 <sup>12</sup>	3318	8.4 x 10 <sup>16</sup>	41.8
63B	Cr-n <sup>+</sup> /Si* (A-141)	200	5.0 x 10 <sup>12</sup>	4053	1.8 x 10 <sup>17</sup>	72.4
10A	Si (LD)	200	5.0 x 10 <sup>12</sup>	3220	1.8 x 10 <sup>17</sup>	73.6
100	(5-μm)In <sup>-</sup> /Si*	200	5.0 x 10 <sup>12</sup>	4005	1.7 x 10 <sup>17</sup>	67.2
45A	(3-μm)In <sup>-</sup> /Si* (C265)	250	7.0 x 10 <sup>12</sup>	4364	1.4 x 10 <sup>17</sup>	40.9
45E	Si (MX)	250	7.0 x 10 <sup>12</sup>	4067	1.5 x 10 <sup>17</sup>	46.9
46F	(10-μm)Cr-n <sup>+</sup> /Si* (A90)	250	7.0 x 10 <sup>12</sup>	4331	1.2 x 10 <sup>17</sup>	37.1
19X	Si (LD)	200	7.0 x 10 <sup>13</sup>	3219	3.7 x 10 <sup>17</sup>	73.0
14C	Si (LD)	200	1.5 x 10 <sup>13</sup>	3230	2.5 x 10 <sup>17</sup>	32.8
64A	Si (MMG102)	200	2.0 x 10 <sup>13</sup>	2699	5.8 x 10 <sup>17</sup>	58.3
57	Si (XS3761)	200	1.0 x 10 <sup>14</sup>	3201	1.5 x 10 <sup>18</sup>	30.6
50A	Si (XS3761F)	200	5.0 x 10 <sup>14</sup>	2691	1.7 x 10 <sup>18</sup>	6.7

\*Vapor-phase high-resistivity epitaxial layer grown on Si substrate.



The implantations listed were for an energy level of 200 keV and a dosage level between  $4 \times 10^{12}$  and  $5 \times 10^{14}$  at./cm<sup>2</sup>. Table 2 lists results on typical Si-implanted samples. All the samples listed were annealed at 825°C for 20 min using the capless process described earlier. The mobility values are in the 3000- to 4400-cm<sup>2</sup>/V-s range, and the activation efficiencies are in the 20 to 80% range.

The lower value of activation occurring in high-dose implanted samples is believed due to the solid solubility limit at the annealing temperature. The mobilities are generally higher ( $\sim 4000$  cm<sup>2</sup>/V-s) for implantations into a high-resistivity epitaxial buffer layer grown on a SI GaAs substrate, as shown in Tables 1 and 2. A direct implant into some substrates (e.g., sample A26, A28C) also gives an electron mobility of higher than 4000 cm<sup>2</sup>/V-s at the  $1-2 \times 10^{17}$ /cm<sup>3</sup> doping density level.

The carrier concentration values listed in Tables 1 and 2 were approximately determined from

$$N_m = \frac{N_S}{\sqrt{2\pi} \Delta R_p} \quad (6)$$

which is an approximation to the Gaussian distribution:

$$N_S = \int_0^\infty N(x,E) dx = \sqrt{\frac{\pi}{2}} N_m \Delta R_p \left[ 1 + \operatorname{erf} \left( \frac{R_p}{\sqrt{2} \Delta R_p} \right) \right] \quad (7)$$

where  $R_p$  and  $\Delta R_p$  are, respectively, the projected range and standard deviation of the implanted atoms. The measured sheet electron concentration values were used for  $N_S$  in Eq. (6), and the  $\Delta R_p$  was taken as 0.08  $\mu$ m at the 200-keV energy level, which is close to that measured by SIMS. Some data computed by Gibbons et al. [23] on the  $R_p$  and  $\Delta R_p$  of <sup>32</sup>S and <sup>28</sup>Si ions implanted into GaAs are reproduced in Table 3.

The mobility versus carrier concentration data of S- and Si-implanted samples were plotted in Figs. 1 and 2, respectively. Theoretical curves [24] of drift mobility with different compensation ratio values are also included

23. J. F. Gibbons et al., "Projected Range Statistics," (Halsted Press, A division of John Wiley and Sons, Inc., New York, 1975).
24. D. L. Rode and S. Knight, "Electron Mobility in GaAs," Phys. Rev. **B3**, 2534 (1971).

TABLE 2. Si IMPLANTATION IN GaAs

SAMPLE NUMBER	SUBSTRATE	ENERGY (keV)	DOSE (cm <sup>-2</sup> )	MOBILITY (cm <sup>2</sup> /V-s)	APPROX CARRIER CONC. (cm <sup>-3</sup> )	ACTIVATION EFF. (%)
A24A	5 $\mu$ m <sup>+</sup> /Si <sup>+</sup> (D96)	200	3.0 $\times 10^{12}$	4265	8.2 $\times 10^{16}$	54.9
A36A	Si (XS3761)	200	3.0 $\times 10^{12}$	3374	1.9 $\times 10^{17}$	82.6
		70	1.5 $\times 10^{12}$			
A36C	Si (XS3766F)	200	3.0 $\times 10^{12}$	3830	1.7 $\times 10^{17}$	76.8
		70	1.5 $\times 10^{12}$			
A36D	5 $\mu$ m <sup>+</sup> /Si <sup>+</sup> (D143)	200	3.0 $\times 10^{12}$	4000	1.9 $\times 10^{17}$	85.1
		70	1.5 $\times 10^{12}$			
A28N	Si (XS3761F)	200	3.5 $\times 10^{12}$	3740	1.6 $\times 10^{17}$	90.3
A23A	Cr <sup>+</sup> /Si <sup>+</sup> (A156)	200	4.0 $\times 10^{12}$	3928	1.2 $\times 10^{17}$	60.5
A3A	Si (NMG102)	200	4.0 $\times 10^{12}$	3570	1.2 $\times 10^{17}$	62.0
A26	Si (XS3765)	200	4.0 $\times 10^{12}$	4000	1.5 $\times 10^{17}$	60.5
		50	2.0 $\times 10^{12}$			
A4B	Si (XS3761)	200	6.0 $\times 10^{12}$	3222	1.9 $\times 10^{17}$	64.7
A31	Si (XS3761)	200	2.0 $\times 10^{13}$	2931	7.0 $\times 10^{17}$	70.1
A6	Si (NMG102)	200	5.0 $\times 10^{13}$	2049	1.1 $\times 10^{18}$	37.0
A34	Si (XS3761F)	200	1.0 $\times 10^{14}$	2204	1.1 $\times 10^{18}$	21.5
A44	Si (XS3761F)	70	1.0 $\times 10^{15}$	1770	1.6 $\times 10^{18}$	3.2

\*Vapor-phase high-resistivity epitaxial layer grown on Si substrate.

TABLE 3. LSS RANGE STATISTICS OF Si AND S IMPLANTATION IN GaAs  
(From J. F. Gibbons et al. [24])

S in GaAs			Si in GaAs		
Energy (keV)	$R_p$ ( $\mu m$ )	$\Delta R_p$ ( $\mu m$ )	Energy (keV)	$R_p$ ( $\mu m$ )	$\Delta R_p$ ( $\mu m$ )
10	0.0094	0.0066	10	0.0103	0.0074
50	0.0375	0.0222	50	0.0424	0.0254
70	0.0518	0.0291	70	0.0592	0.0333
100	0.0740	0.0387	100	0.0850	0.0442
120	0.0891	0.0448	120	0.1025	0.0510
150	0.1121	0.0534	150	0.1291	0.0607
200	0.1509	0.0667	200	0.1739	0.0753
250	0.1901	0.0788	250	0.2187	0.0884
300	0.2292	0.0899	300	0.2632	0.1003
400	0.3067	0.1096	400	0.3507	0.1210
600	0.4569	0.1412	600	0.5181	0.1534
800	0.5996	0.1658	800	0.6750	0.1780
1000	0.7349	0.1856	1000	0.8225	0.1975

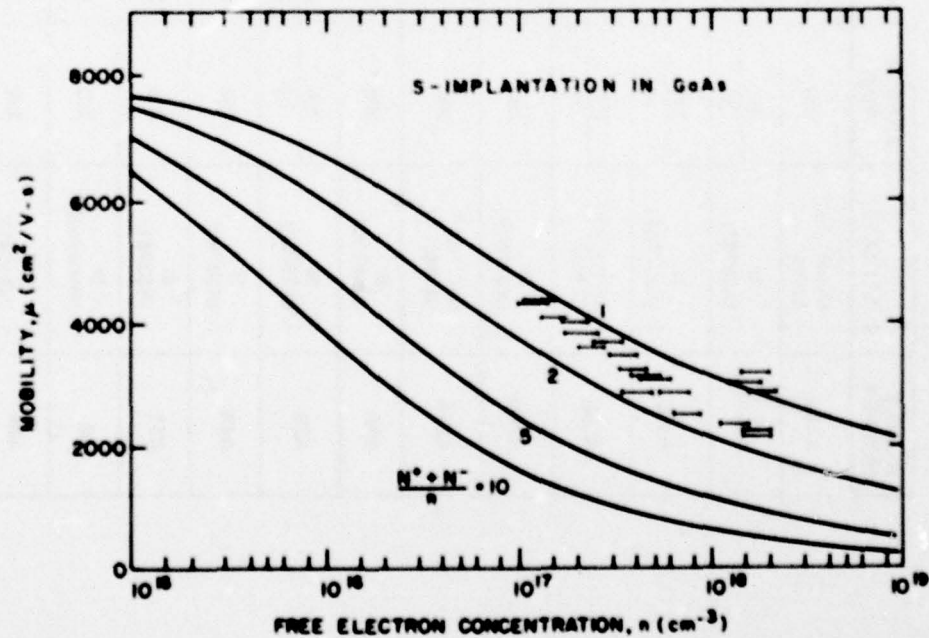


Figure 1. Mobility vs carrier concentration, S implanted in GaAs.



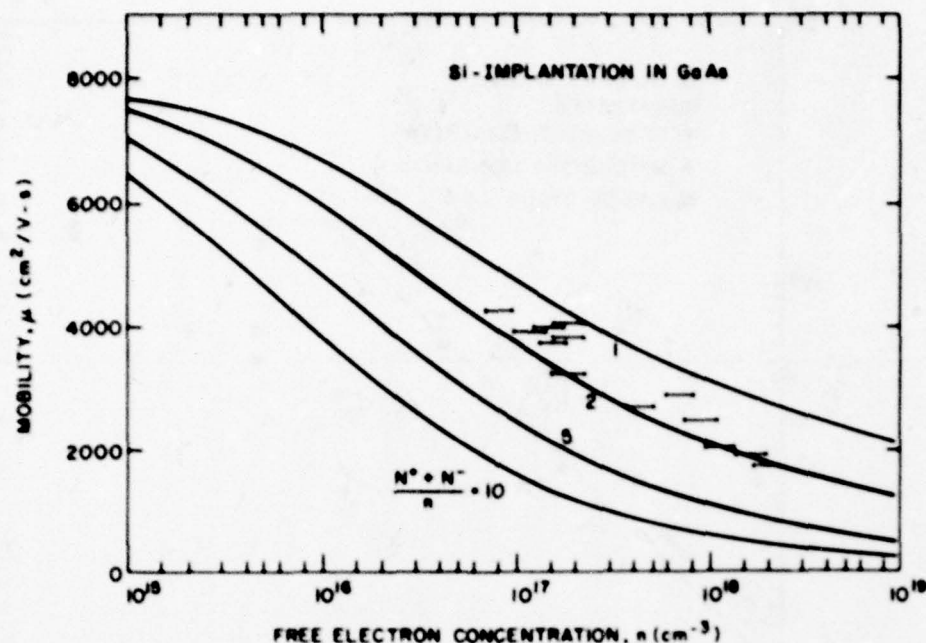


Figure 2. Mobility vs carrier concentration, Si implanted in GaAs.

in the plots. Most of our experimental data points are located between a compensation ratio of 1 and 2, indicating that material quality is acceptable.

Experimental data of carrier concentration (electrically activated) as a function of implantation dose are shown in Fig. 3 for S implantation into GaAs, and in Fig. 4 for Si implantation into GaAs. The samples were capless-annealed at a temperature of 825°C for 20 min. The implantation energy was 200 keV for all data points. Scattering of data points for different substrate materials is present in the plot. The data in both the Si- and S-implantation cases indicate the following features. (1) In the range of fluence between  $5 \times 10^{12}$  and  $3 \times 10^{13}$  at./cm<sup>2</sup> for S implant, and  $2.5 \times 10^{12}$  and  $2 \times 10^{13}$  at./cm<sup>2</sup> for Si implant, the carrier concentration varies approximately linearly with the fluence; (2) the free carrier concentration increases at a much slower rate at a high fluence level. This might be expected as it approaches the solubility limit. A thermal annealing of up to 1000°C for 20 min has been carried out as shown by the unfilled circle in Fig. 4. The sheet carrier concentration increases somewhat, but it still stays in the low increasing rate range. The high-temperature anneal was done in nitrogen atmosphere with samples encapsulated with 2000 Å of sputtered Si<sub>3</sub>N<sub>4</sub>. The electrical activation is much higher in

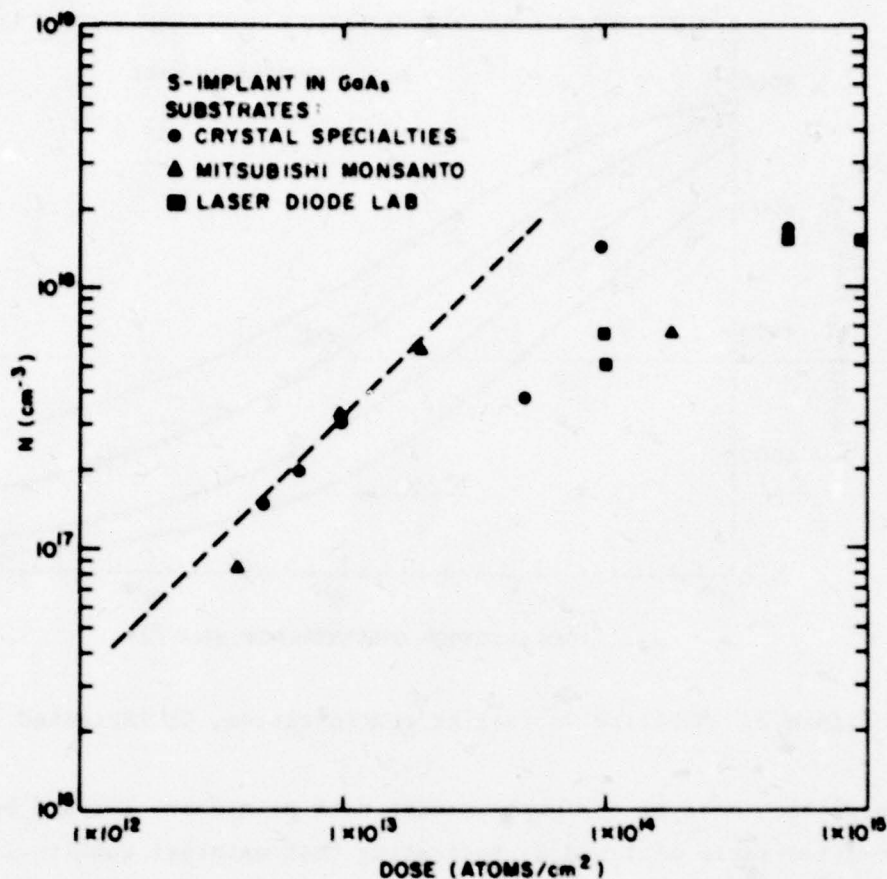


Figure 3. Carrier concentration as a function of implantation dose for S implantation into GaAs.

laser-annealed samples which will be described in Section IV. Similar saturation effect for Se and S implantations have been reported by Donnelly [25]; and (3) no electrical activations were observed when the GaAs substrate was implanted at a low-dose level. At the implantation energy of 200 keV, a typical lower limit was around  $2 \times 10^{12}$  at./cm<sup>2</sup>. This "cut-off" threshold varies with substrate material. The mechanism of this cut-off behavior is not fully understood at present.

25. J. P. Donnelly, "Ion Implantation in GaAs," 1976 North American Symposium on GaAs and Related Compounds.

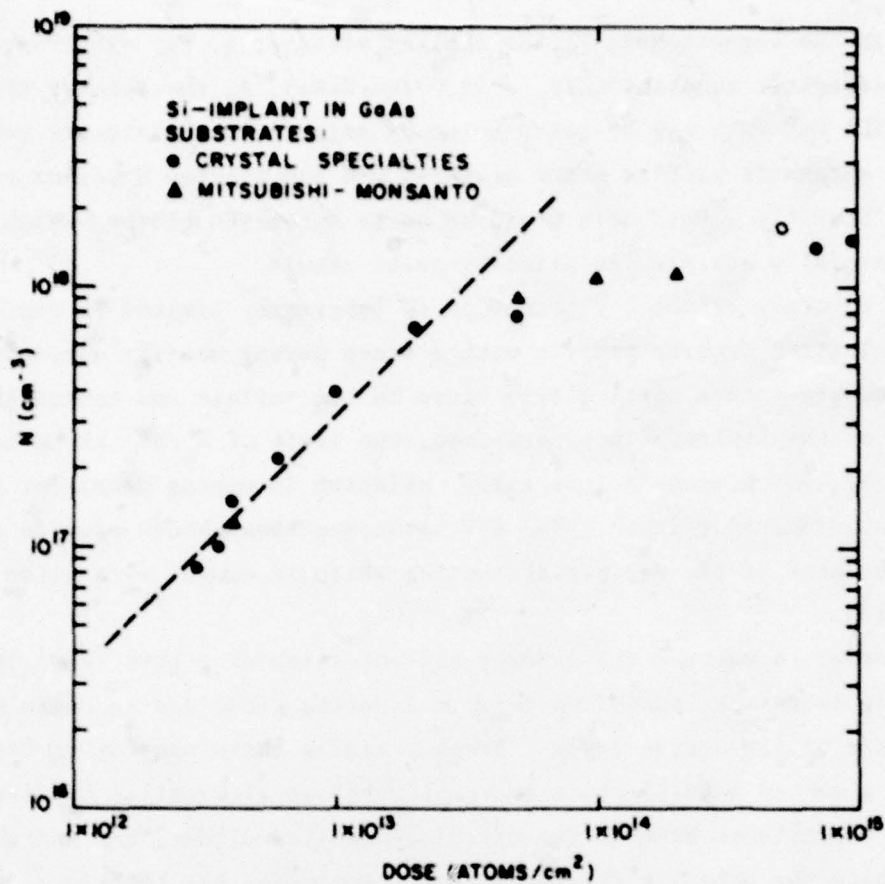


Figure 4. Carrier concentration as a function of implantation dose for Si implantation into GaAs.

## 2. Depth Distribution of Electron Concentration

From reverse-biased capacitance versus applied voltage data on a Schottky diode of known area, the depth distribution of charged carriers can be computed from [26]

$$N = \frac{-C^3}{q\epsilon A^2} \left( \frac{\partial C}{\partial V} \right)^{-1} \quad (13)$$

and

$$x = \epsilon \frac{A}{C} \quad (14)$$

26. C. O. Thomas, D. Kahng, and R. C. Manz, "Impurity Distribution in Epitaxial Silicon Films," J. Electrochem. Soc. 109, 1055 (1962).



where  $C$  is the capacitance;  $V$ , the applied voltage;  $q$ , the electronic charge;  $\epsilon$ , the dielectric constant ( $\epsilon/\epsilon_0 = 12.5$  for GaAs);  $A$ , the area of the Schottky diode. The C-V data may be taken point by point on a capacitance bridge, or using an automatic plotter which measures C-V and plotted  $N$  versus  $x$  on an x-y recorder directly. Data were measured on an automatic plotter which was calibrated carefully against the point-by-point result.

The accuracy of the C-V technique is inherently limited in reproducing a shallow electron density profile with a steep doping density variation [27]. The inaccuracy occurs particularly close to the surface and toward the tail end. For most of the implantations performed, the ratio of  $R_p/\Delta R_p$  is on the order of 2 (Table 3), which means a less steep variation in doping densities as compared to implantations in silicon. The C-V technique thus should provide information around the peak of the depth distribution which is useful as a guide to device fabrication.

In order to measure the carrier concentration of a thin layer on a semi-insulating substrate, one often forms a Schottky diode and an ohmic contact on the surface of the active layer. Because making ohmic contact to GaAs usually requires a second metallization and sintering, an alternative way simply measures the capacitance between two circular Schottky diodes, one being forward-biased while the other is reverse-biased. Applying this technique, however, introduces an additional zero-bias capacitance connecting in series with the reverse-biased capacitance. This must be corrected according to

$$1/C = 1/C_r + 1/C_f \quad (15)$$

where  $C$  is the measured capacitance,  $C_r$  the reverse-biased capacitance, and  $C_f$  the forward-biased capacitance.

A technique was developed [28] in preparing samples for C-V measurement which eliminates the above complexities. Figure 5 shows the patterns of Schottky contact made to the active implanted layer. The circular diodes are surrounded by large-area Schottky contacts forming a donut-shaped pattern.

27. C. P. Wu, E. C. Douglas, and C. W. Mueller, "Limitations of the CV Technique for Ion-Implanted Profiles," IEEE Trans. on Electron. Devices 22, 319 (1975).
28. S. G. Liu, to be published.

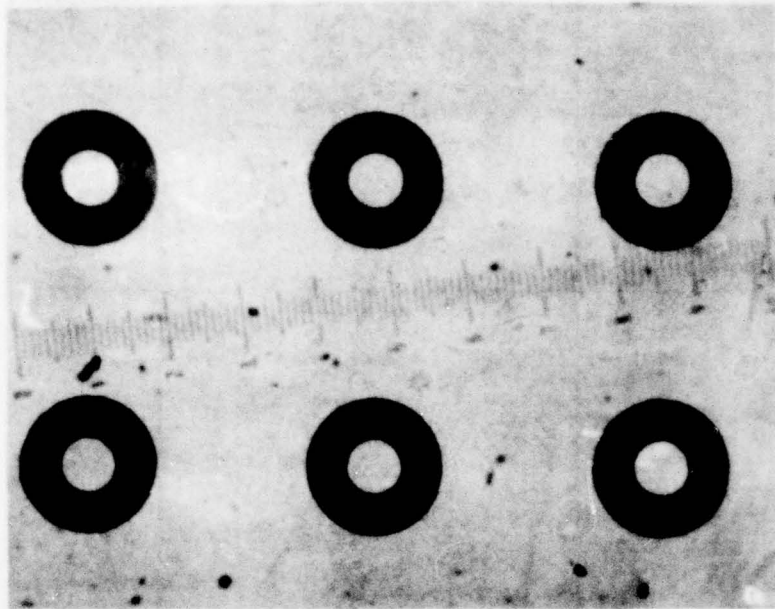


Figure 5. Photograph showing patterns of Schottky contact.

Because of the large-area Schottky contact, the capacitance  $C$  measured between the reverse-biased circular diode and the forward-biased Schottky contacts approximately equals  $C_r$ , since the second term in Eq. (15) can be neglected. No corrections are therefore required in measured capacitance data. Samples prepared in this manner are readily adaptable to the automatic C-V profile equipment.

The Schottky patterns shown in Fig. 5 were easily produced by a single-step photolithography, followed by metallization and lift-off. Cr-Au (500-Å Cr/1500-Å Au), Ti-Pt-Au (500-Å Ti/500-Å Pt/1500-Å Au) or Al (2000 Å) metallization was used in forming Schottky contacts for C-V measurement. The diameter of the circular dots is 0.152 mm (0.006 in.) which produces a zero-bias capacitance below 30 pF for a typical implanted layer. This capacitance value is within the limit of the automatic C-V profile equipment.

Figure 6 shows the carrier-concentration density profile of a Si-implanted sample (A49A) as measured on the automatic C-V impurity profile equipment. The implantation dose and energy level are  $3.5 \times 10^{12}$  at./cm<sup>2</sup> and 200 keV, respectively.

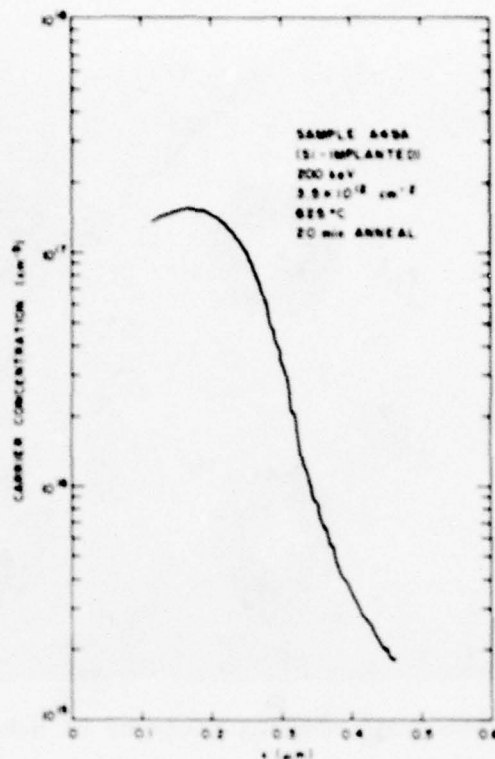


Figure 6. Carrier concentration profile for single-energy Si implant.

Figure 7 shows the carrier-concentration density profile of a multiple Si-implanted sample (A 60B) obtained from C-V measurement. The dose and energy levels of the double implantations are  $3 \times 10^{12}$  at./cm<sup>2</sup>, 200 keV, and  $1 \times 10^{12}$  at./cm<sup>2</sup>, 70 keV, which are designed to yield a nearly constant doping distribution. Figure 7 demonstrates that the implantation profile can be controlled by using multiple implants.

The measured electron distribution of S-implanted GaAs is usually broader than for Si-implanted samples, and deviates from a Gaussian distribution. This may be attributed to a significant diffusion effect during anneal. Figure 8 shows a measured curve with circles indicating the LSS distribution, including the thermal diffusion effect, normalized to match the peak of the measured curve. The diffusion coefficient corresponding to the 825°C anneal temperature was deduced from the matched curve to be  $5 \times 10^{-14}$  cm<sup>2</sup>/s. Similar measurements on a number of samples show a range of between  $2 \times 10^{-14}$  and  $5 \times 10^{-14}$  cm<sup>2</sup>/s under this anneal condition. This value compares favorably with those measured by



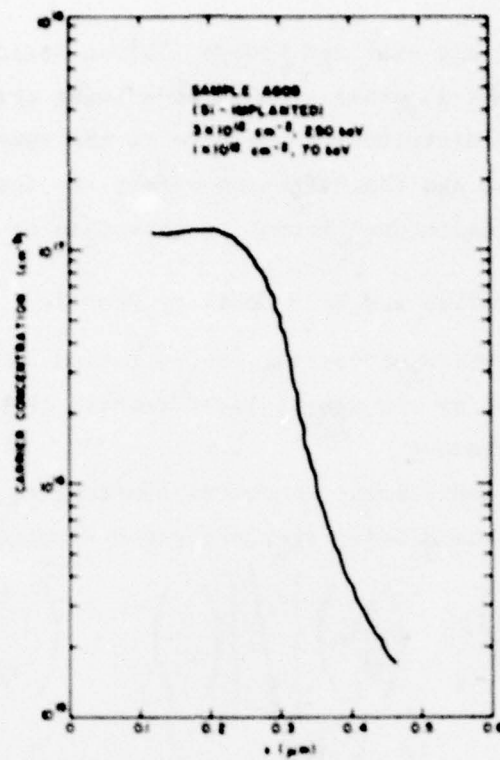


Figure 7. Carrier concentration profile for dual Si implant.

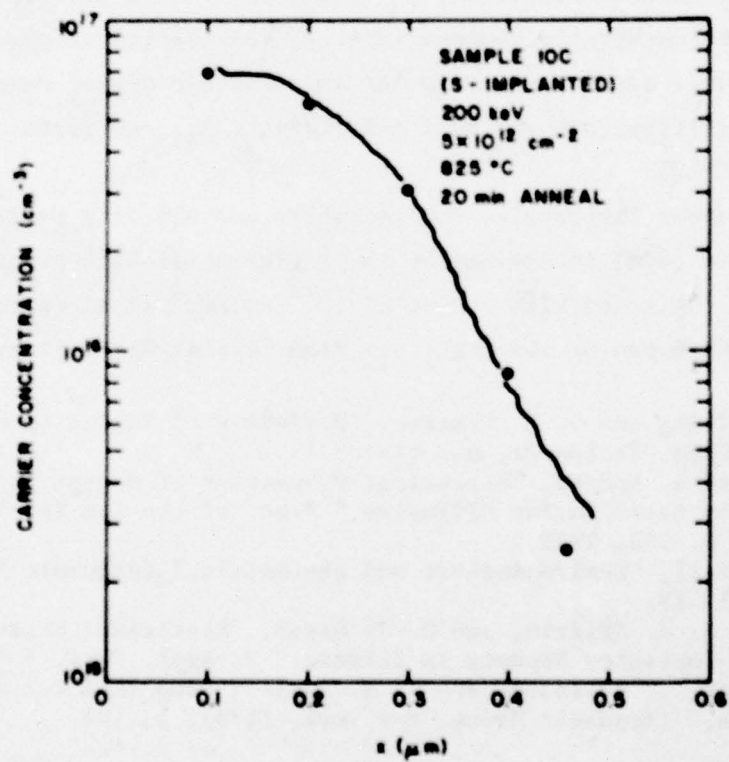


Figure 8. Measured electron density distribution of S-implanted GaAs.

Young and Pearson [29] and Asai and Kodera [30] on solid-state S diffusion into bulk GaAs, but is almost an order of magnitude lower than Kendall's result [31]. A similar match of LSS distribution was made to the measured profile on Si-implanted GaAs samples, and the diffusion effect was found to be negligible. The corresponding diffusion coefficient is less than or equal to  $10^{-15} \text{ cm}^2/\text{s}$ .

### 3. Electron Concentration and Hall Mobility Profile

The depth distribution of carrier concentration and mobility on some samples were determined by the use of layer removal technique combined with the van der Pauw measurement.

The mobility,  $\mu$ , and carrier concentration density,  $n$ , corresponding to the  $i$ -th chemically removed GaAs layer are given respectively by [32,33]

$$\mu_i = \left[ \left( \frac{R_S}{\rho_s^2} \right)_{i-1} - \left( \frac{R_S}{\rho_s^2} \right)_i \right] / \left[ \left( \frac{1}{\rho_s} \right)_{i-1} - \left( \frac{1}{\rho_s} \right)_i \right] \quad (16)$$

$$n_i = \left[ \left( \frac{1}{\rho_s} \right)_{i-1} - \left( \frac{1}{\rho_s} \right)_i \right] / q h_i \mu_i \quad (17)$$

where  $\rho_s$  is the sheet resistivity,  $R_S$  is the sheet Hall coefficient,  $h$  the thickness of the chemically removed layer,  $q$  the electrical charge, and the lower case index  $i$  and  $i-1$  refer to the successive order of removed layer. The sheet resistivity,  $\rho_s$ , and Hall coefficient,  $R_S$ , are given, respectively, by Eqs. (3) and (2).

Figure 9 shows the carrier concentration and mobility profile of a S-implanted sample (49B) determined by the differential Hall-effect measurement. The sample was implanted with a dose of  $10^{13} \text{ at./cm}^2$  at an energy level of 200 keV. The Cr-doped SI substrate was from Crystal Specialties. Post-implant

29. A. B. Y. Young and G. L. Pearson, "Diffusion of Sulfur in GaP and GaAs," *J. Phys. Chem. Solids* **31**, 517 (1970).
30. S. Asai and H. Kodera, "Electrical Properties of n-type Layers in GaAs prepared by Solid Sulfur Diffusion," *Proc. of the 4th Int. Symp.*, Boulder, Colorado, p. 130, 1972.
31. P. L. Kendall, "Semiconductors and Semimetals," (Academic Press, New York, 1968), Vol. IV.
32. R. Baron, G. A. Shifrin, and O. J. Marsh, "Electrical Behavior of Group III and V Implanted Dopants in Silicon," *J. Appl. Phys.* **40**, 3702 (1969).
33. J. W. Mayer, L. Eriksson, and J. A. Davies, "Ion Implantation in Semiconductors," (Academic Press, New York, 1970), p. 193.

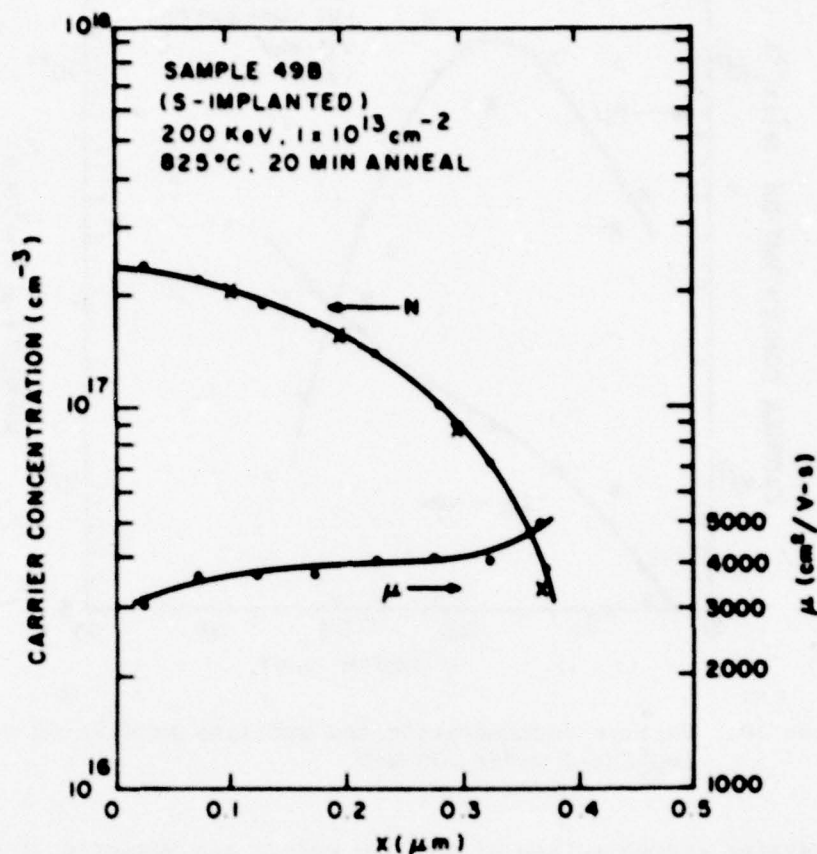


Figure 9. Carrier concentration and mobility profile of a S-implanted sample.

annealing was done at 825°C for 20 min under  $\text{AsH}_3$  overpressure as described earlier. The profile shows a maximum carrier concentration of  $2.4 \times 10^{17} / \text{cm}^3$  which agrees with that obtained by C-V measurement. The mobility profile varies from  $3000 \text{ cm}^2/\text{V-s}$  at the surface to over  $4000 \text{ cm}^2/\text{V-s}$  toward the SI substrate, which agrees with the measured effective Hall mobility of  $3520 \text{ cm}^2/\text{V-s}$  for the entire implanted layer.

The profile deduced from the C-V measurement after normalization in carrier concentration matches well with the profile measured by differential Hall-effect measurement. The normalized points are indicated as crosses in Fig. 9. Both cases are for S implantation at 200 keV but with a difference in implanted dosage.

The carrier concentration and mobility profiles on two high-dose Si-implanted GaAs wafers are shown in Figs. 10 and 11. The average mobility



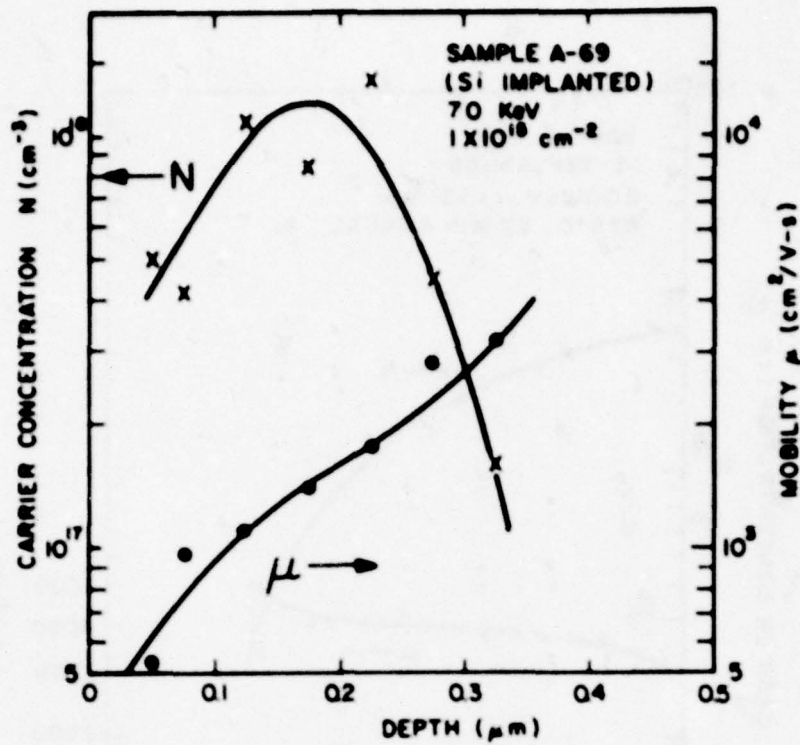


Figure 10. Carrier concentration and mobility profile of a Si-implanted wafer, 70 keV.

and sheet carrier concentration of the two wafers are measured to be, respectively,  $1800 \text{ cm}^2/\text{V-s}$  and  $2.14 \times 10^{13} \text{ at./cm}^2$  for sample A69, and  $2120 \text{ cm}^2/\text{V-s}$  and  $2.26 \times 10^{13} \text{ at./cm}^2$  for sample A82. Layers of GaAs were etched using  $\text{H}_2\text{SO}_4:\text{H}_2\text{O}_2:\text{H}_2\text{O}$  in the ratio 1:1:50 at  $0^\circ\text{C}$ . This gave an etch rate of  $4.4 \text{ \AA/s}$ .

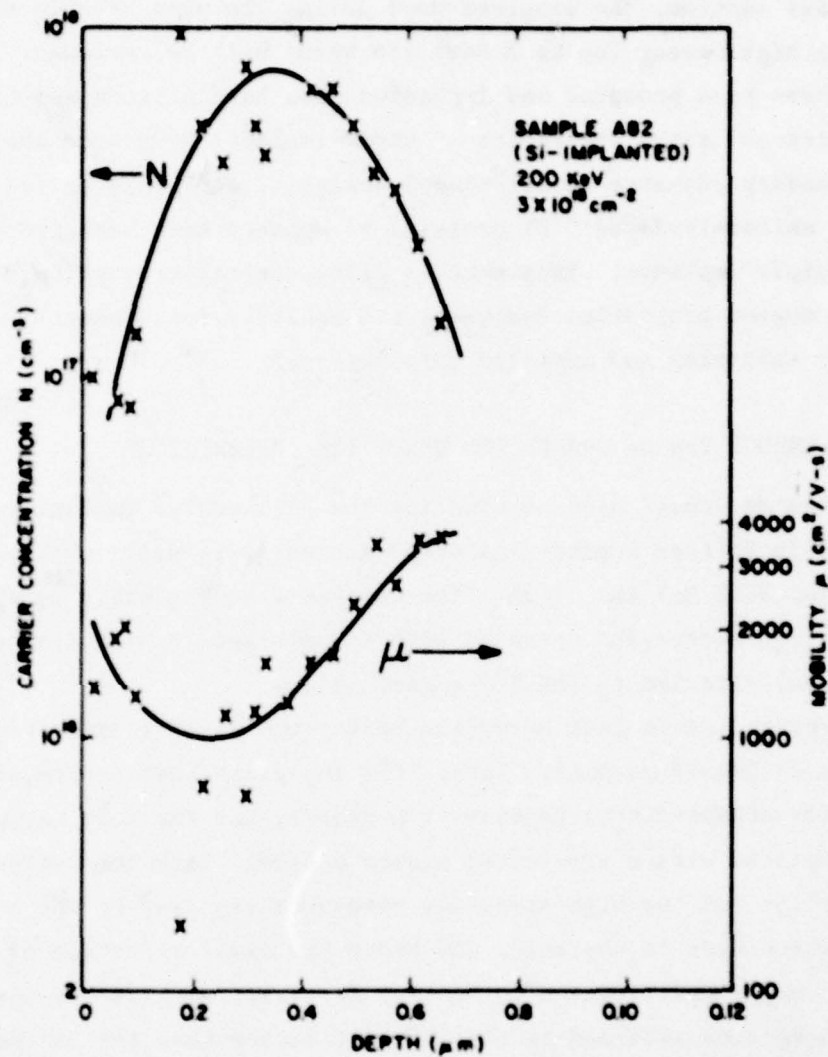


Figure 11. Carrier concentration and mobility profile of a Si-implanted wafer, 200 keV.

## SECTION III

### HIGH-ENERGY (UP TO 1.2 MeV) IMPLANTATION

In this section, the progress made during the past year in obtaining and implanting high-energy (up to 3 MeV) ion beams will be reviewed. Beams of  $^{11}\text{B}$  and  $^{28}\text{Si}$  have been produced and implanted into both silicon and GaAs substrates. The profiles and range statistics of these implants have been analyzed using SIMS (secondary ion-mass spectroscopy) analysis, and based on the information obtained, uniformly doped  $^{28}\text{Si}$  profiles  $\sim 1\text{ }\mu\text{m}$  deep have been produced in GaAs using multiple implants. This section discusses the production of implanted profiles, dopant activation analyses, and mobility measurements on implanted (single or multiple) and annealed GaAs wafers.

#### A. HIGH-ENERGY Van de GRAAFF FOR HEAVY ION IMPLANTATION

The Van de Graaff machine used for the high-energy implant experiments was built by High Voltage Engineering Corp\* and was originally designed to produce proton beams at 3 MeV and  $\sim 1\text{ mA}$ . The machine was originally equipped with a duo-plasmatron source and operated with a cumbersome end-station (for wafer implantation) attached to the  $25^\circ$  magnet port.

To produce and implant heavy ion beams, two major modifications were made to the Van de Graaff machine. First, the duo-plasmatron source was replaced with a cold-cathode-discharge heavy ion source, and the cold cathode source was in turn replaced with a rf-excited plasma source. Both the extraction optics on the machine and the high operating pressures required by the available cold cathode source made it unusable, and hence the final selection of the rf source. The second major modification to the Van de Graaff machine was the construction of a new beam line attached to the  $15^\circ$  port rather than the  $25^\circ$  port of the analyzing magnet. Using the  $15^\circ$  port, a mass-energy (at mass  $\times$  energy in MeV) product of  $\sim 33$  could be achieved with the available analyzing magnet. The new beam line that was constructed contained x-y sweep plates and terminated in an end-station which holds a single wafer at a time. The implant area is  $\sim 2.54\text{ cm}$  by  $2.54\text{ cm}$ . During the implant, the normal to the wafer was inclined at an angle of  $7^\circ$  relative to the direction of the incident beam. The vacuum in the

\*High Voltage Engineering Corp, Burlington, MA.



beam line and end-station during the implant was maintained in the  $10^{-6}$ -Torr region.

#### B. CALIBRATION IMPLANTS USING $^{11}\text{B}^+$ BEAM

The first experiments were performed using  $\text{BF}_3$  as a source gas in the ion source and implanting  $^{11}\text{B}^+$  ions into a silicon substrate. These conditions were chosen because the spectrum of  $\text{BF}_3$  (i.e., the amplitude of the various ion components extracted from the source plotted as a function of the current in the analyzing magnet) is well known and has a distinctive set of  $^{10}\text{B}^+$ ,  $^{11}\text{B}^+$  peaks. The mass of the boron ion is also relatively small so the machine could be exercised at higher energies. The mass-energy product (atomic mass x energy in MeV) for the machine is  $\sim 33$ .  $^{11}\text{B}$  in silicon was also selected for the first tests because of the ability of SIMS analysis to readily measure the profile.

Figure 12 shows a SIMS plot of a 1-MeV  $^{11}\text{B}$  implant that was made on the FEC\* machine compared with a 60-keV  $^{11}\text{B}$  implant that was made on the Princeton Labs implanter. (The SIMS analysis was carried out by C. Magee.) The scanned area in the newly constructed beam line is 2.54 cm x 2.54 cm and all portions of the system performed well during the implant.

To test the endurance of the machine for higher level implants, a series of implants was made at progressively higher energies as shown in the SIMS plots given in Fig. 13. Each implant required approximately 45 min of implant time using a beam current of  $\sim 4 \mu\text{A}$ . These implants were carried out over a two-day period of essentially continuous running. Terminal overheating problems were experienced during these long tests, and suitable corrections were made to some of the cooling systems. Beam currents as high as  $8 \mu\text{A}$  of  $^{11}\text{B}$  were obtained, but lower values were used to prevent excessive end-station and wafer heating. (At 2 MeV and  $8 \mu\text{A}$ , the average incident power density on target is  $\sim 2.5 \text{ W/cm}^2$ .)

The measured value of the range  $R_p$  for the series of  $^{11}\text{B}$  implants is given in Fig. 14. The value of the implant energy was calibrated by bombarding a lithium target with high-energy protons (obtained from the source operating with  $\text{SiH}_4$ ). A resonant interaction occurs between the lithium target and the proton beam at 1.88 MeV which produces detectable neutrons. The machine is

\*Fusion Energy Corporation, Princeton, NJ.

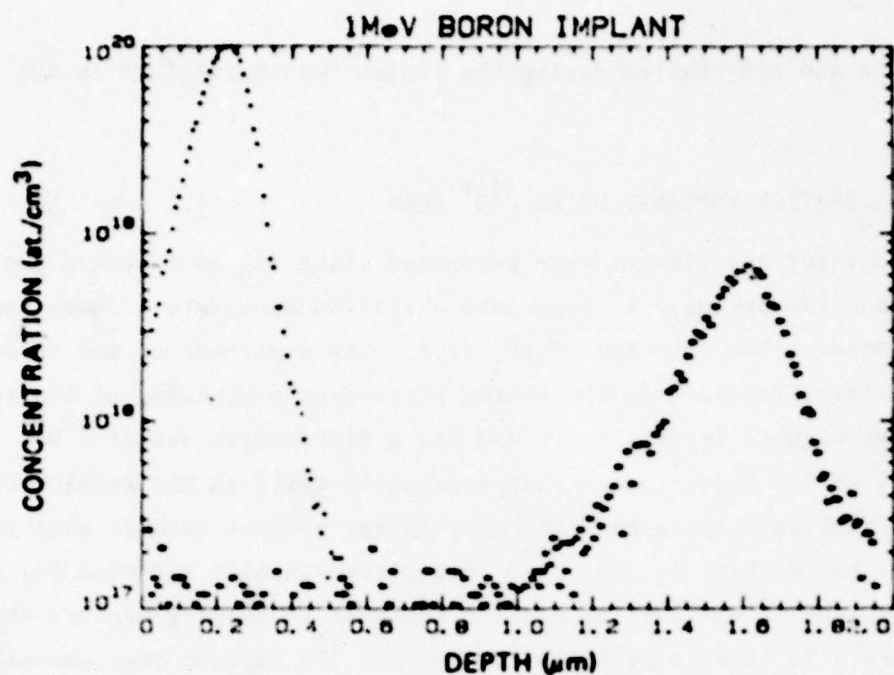


Figure 12. SIMS plots of a 60-keV  $^{11}\text{B}$  implant performed on the Laboratories machine and a 1-MeV  $^{11}\text{B}$  implant performed on the FEC Van de Graaff implanter.

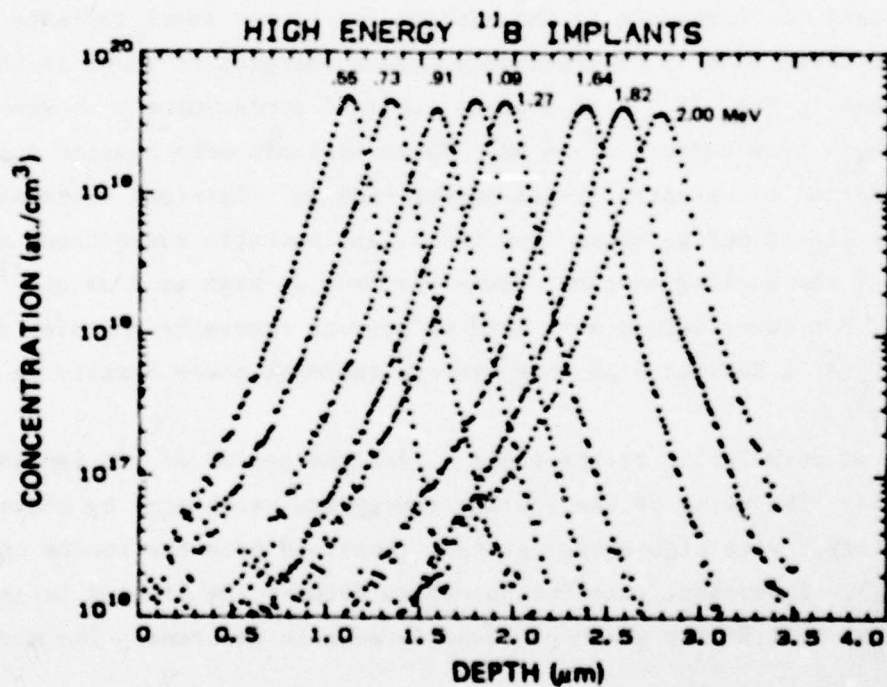


Figure 13. SIMS plots of a group of samples implanted with increasing energies using the FEC Van de Graaff implanter.

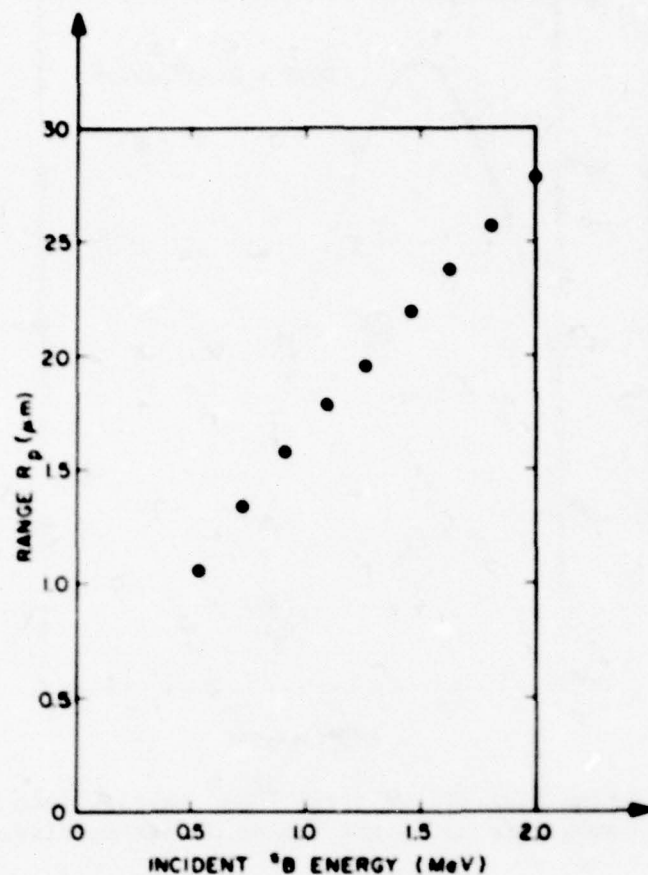


Figure 14. Measured value of the range  $R_p$  for the series of  $^{11}\text{B}$  implants.

calibrated by comparing the reading on the machine energy dial with the occurrence of neutrons being emitted from the lithium target.

### C. IMPLANTATION of $^{28}\text{Si}^+$ INTO GaAs

#### 1. Calibration

Having demonstrated with  $^{11}\text{B}$  the ability of the Van de Graaff machine to produce heavy ion beams, the source gas was changed from  $\text{BF}_3$  to  $\text{SiH}_4$  and beams of  $^{28}\text{Si}^+$  were produced and implanted into GaAs substrates. The results of the first test implants made at 600 keV are shown in the SIMS plot given in Fig. 15. These results indicate that the magnet was properly adjusted to produce a Si beam.



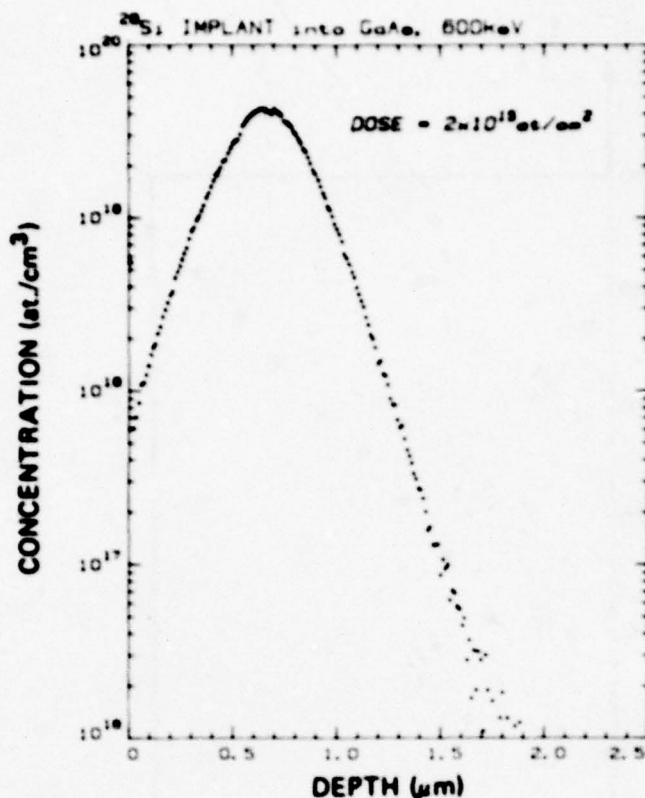


Figure 15. SIMS plot of the first  $^{28}\text{Si}^+$  implant into a GaAs substrate using the Van de Graaff machine.

The results of a series of implants made at a number of different implant energies ranging from 40 keV to 1.2 MeV are shown in Figs. 16 and 17. The lower range implants (40 to 280 keV) were performed on the implant machine located at the Princeton Laboratories and the higher range implants (0.7 to 1.2 MeV) were performed on the Van de Graaff implanter.

Figure 18 shows a set of implants made at different dose levels. There is a discrepancy between the dose specified and the dose actually observed in the wafer. This error could be caused by inaccuracies in the dose measurement system or perhaps could be due to the implantation of  $^{28}\text{N}_2^+$  along with  $^{28}\text{Si}^+$ . A similar dose discrepancy has been observed in the multiple implant profile (described in the next section) and work is underway to resolve this discrepancy.

It is evident from Fig. 17 that the profiles are not Gaussian in shape but are noticeably skewed toward the wafer surface. This is not unexpected for high-energy implants since the conventional LSS theory, which predicts Gaussian

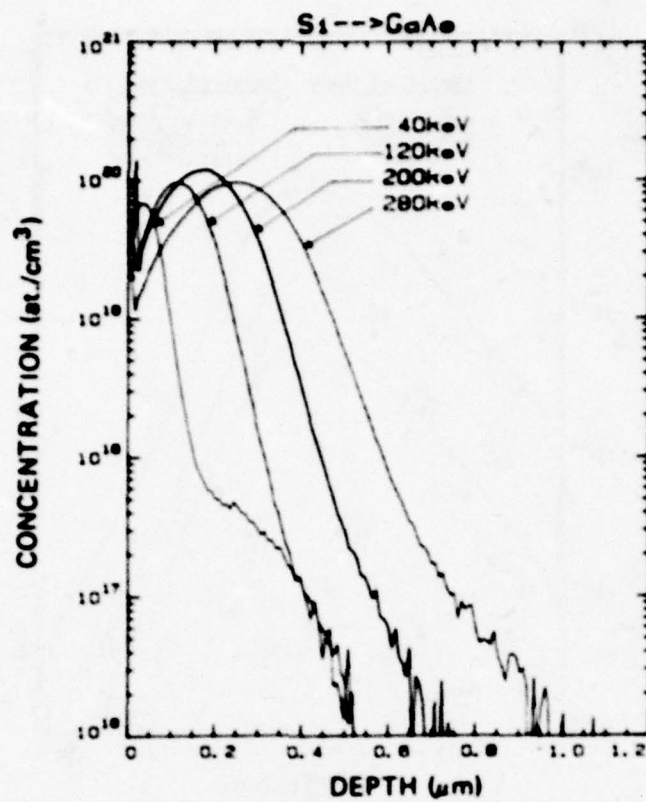


Figure 16. SIMS profiles of implants made at energies of 40, 120, 200, and 280 keV.

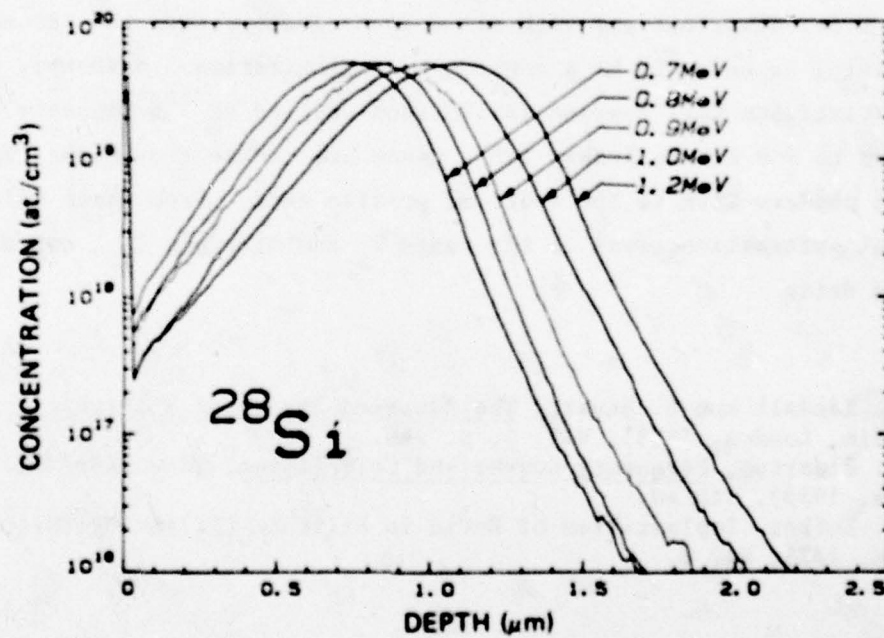


Figure 17. SIMS profiles of implants made at energies of 0.7, 0.8, 0.9, 1.0, 1.2 MeV.

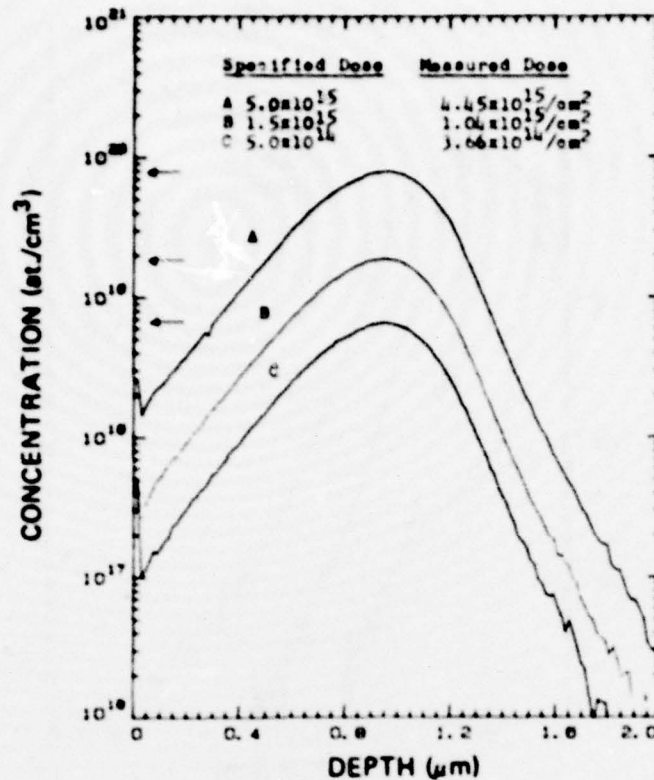


Figure 18. SIMS plots of 1-MeV  $^{28}\text{Si}$  implants made into GaAs at different dose levels.

profiles, i.e., distributions with all moments greater than the second moment equal to zero, is known to be a low-energy approximation. A theory, developed by the statistician Karl Pearson [34,35] and applied to  $^{11}\text{B}$  implants into Si at energies up to 800 keV by Hofker [36], makes use of the first four experimental moments to produce fits to the observed profile data. From these calculations, statistical information, such as the range  $R_p$  and straggle  $\Delta R_p$ , can be obtained for skewed data.

34. M. G. Kendall and A. Stuart, The Advanced Theory of Statistics, (Charles Griffin, London, 1958), Vol. 1, p. 148.
35. W. P. Elderton, Frequency Curves and Correlation, (Cambridge University Press, 1953), 4th ed.
36. W. K. Hofker, Implantation of Boron in Silicon, Philips Research Supplements, 1975, No. 8.



The results of curve fitting to the experimental data, based on the first four experimental moments, are shown in Figs. 19 to 21. Figures 19 and 20 show both a log and a linear plot of the experimental and calculated data using the formula described by Elderton [35]. Figure 21 shows a composite plot of the curves corresponding to the experimental data given in Fig. 17. Figure 22 shows a reduction of the data to  $R_p$  and  $\Delta R_p$  values corresponding to LSS Gaussian reduction techniques and first-four-moment Pearson techniques. It should be noted that the crossovers of the computed curves in Fig. 21 and the poor fit of the computed curves to the extended tails at both the shallow and deep portions of the curve indicate that care must be taken to ensure that excessive channeling is not present. To test this hypothesis, experiments are planned which involve implantation into amorphized substrates.

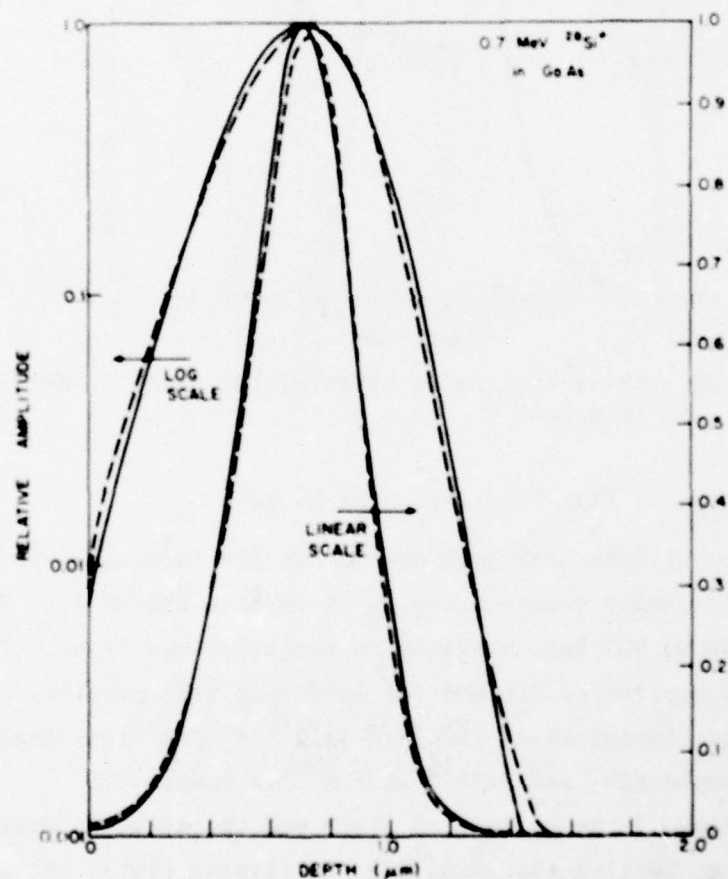


Figure 19. Curve-fitting to experimental data, 0.7-MeV  $^{28}\text{Si}^+$  into GaAs.

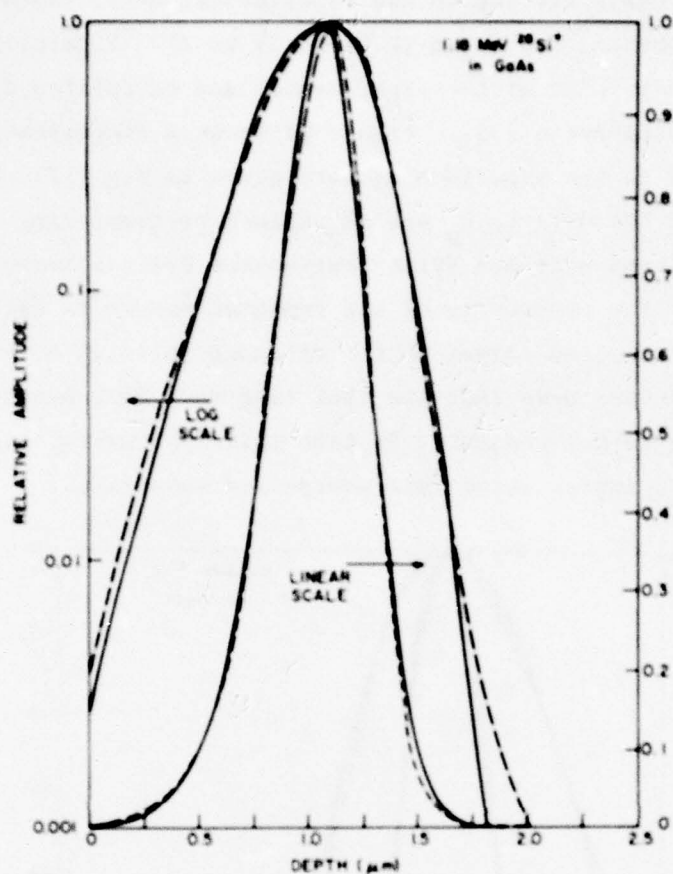


Figure 20. Curve-fitting to experimental data, 1.18-MeV  $^{28}\text{Si}^+$  into GaAs.

## 2. The Formation of Flat Profiles of Si in GaAs

Implant conditions have been worked out for forming  $\sim 1\text{-}\mu\text{m}$ -deep layers of Si in GaAs with nearly constant doping throughout the layer. Five implants, ranging from 40 to 900 keV, are used to construct the layer. Table 4 shows the calculated implant conditions for achieving flat profiles at three different impurity concentration levels:  $1 \times 10^{20}$  at./cm<sup>3</sup> for sample H23,  $2.5 \times 10^{19}$  at./cm<sup>3</sup> for sample H24, and  $1 \times 10^{19}$  at./cm<sup>3</sup> for sample H25.

A comparison of the calculated plot\* and the actually measured SIMS profile is given in Fig. 23 (log plot) and Fig. 24 (linear plot). Actual implantation

\*The calculated data were made using conventional LSS  $R_p$  and  $\Delta R_p$  values because at the time of calculation, the Pearson four-moment-curve fits<sup>P</sup> had not yet been investigated.

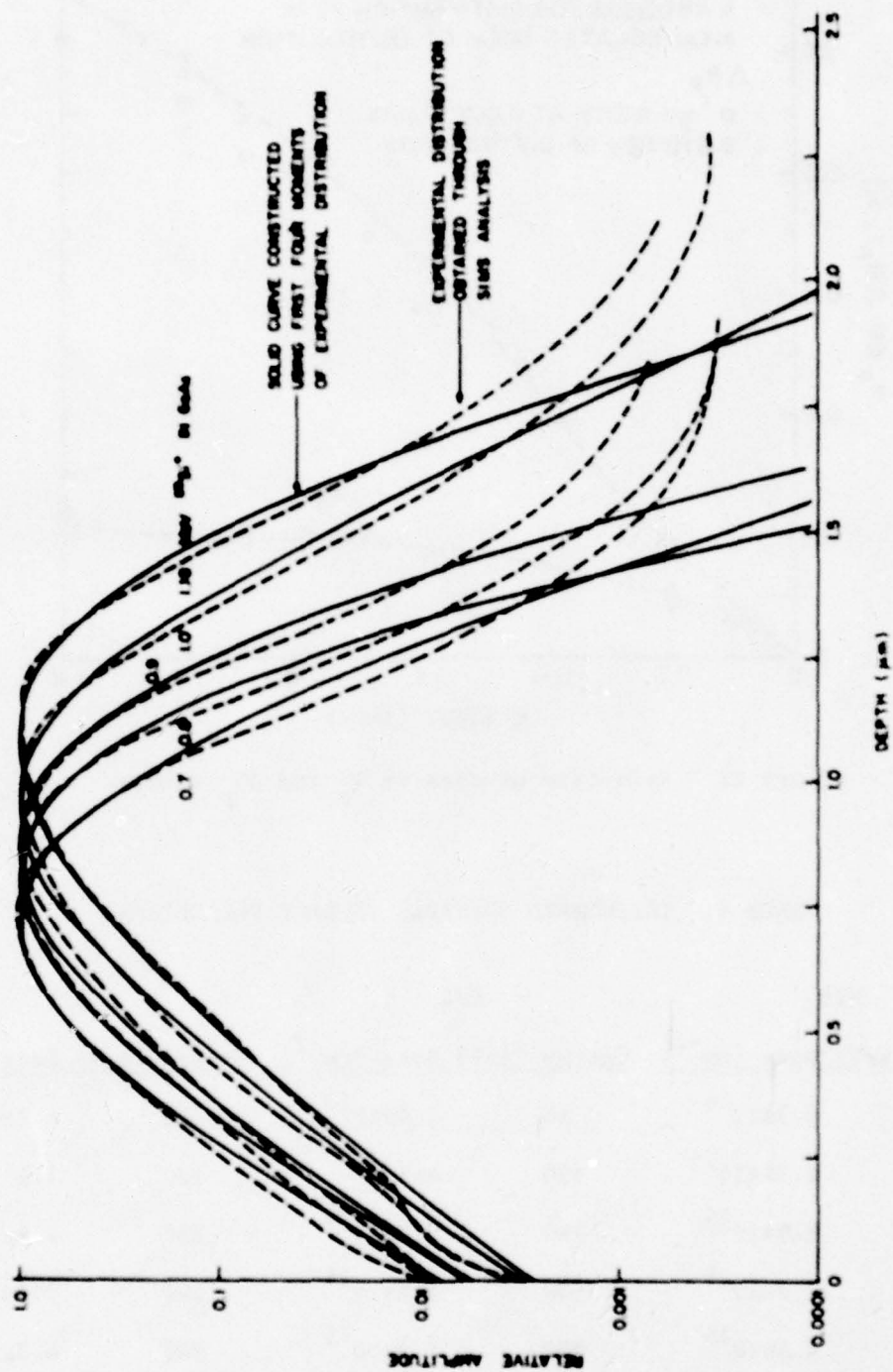


Figure 21. Composite plots of curves corresponding to the data given in Fig. 17.



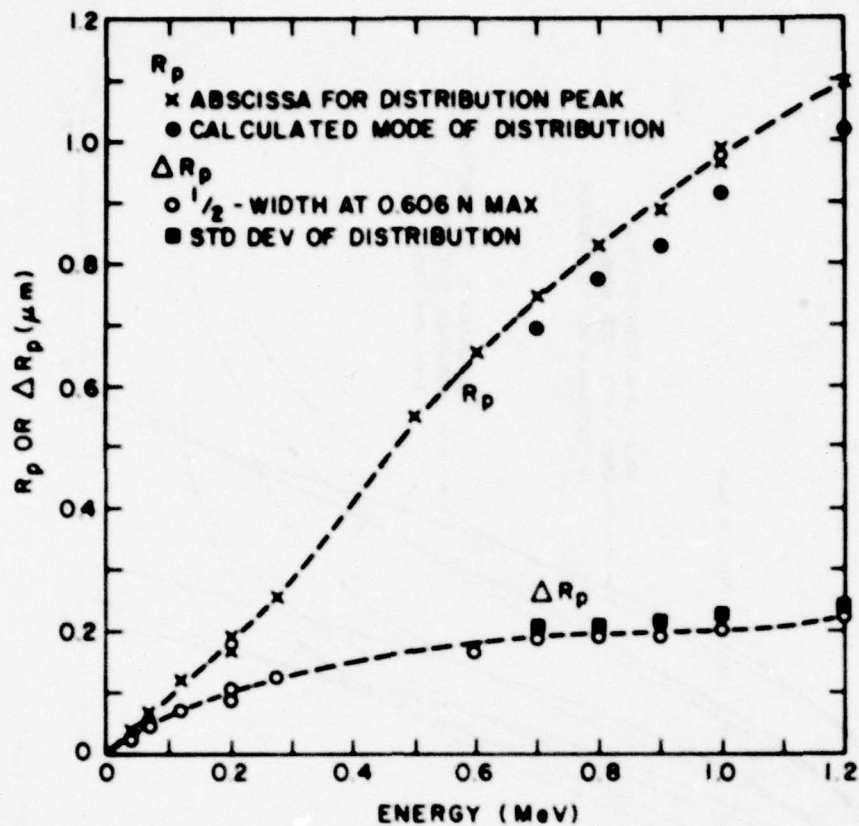


Figure 22. Reduction of data to  $R_p$  and  $\Delta R_p$  values.

TABLE 4. CALCULATED MULTIPLE IMPLANT PARAMETERS

H23		H24		H25	
Energy (keV)	Dose (cm <sup>-2</sup> )	Energy (keV)	Dose (cm <sup>-2</sup> )	Energy (keV)	Dose (cm <sup>-2</sup> )
40	$4.7 \times 10^{14}$	40	$1.4 \times 10^{14}$	40	$4.7 \times 10^{13}$
120	$1.35 \times 10^{15}$	120	$4 \times 10^{14}$	120	$1.35 \times 10^{13}$
280	$1.9 \times 10^{15}$	280	$5.7 \times 10^{14}$	280	$1.9 \times 10^{14}$
500	$2.7 \times 10^{15}$	500	$8.2 \times 10^{14}$	500	$2.7 \times 10^{14}$
900	$4.3 \times 10^{15}$	900	$1.3 \times 10^{15}$	900	$4.3 \times 10^{14}$

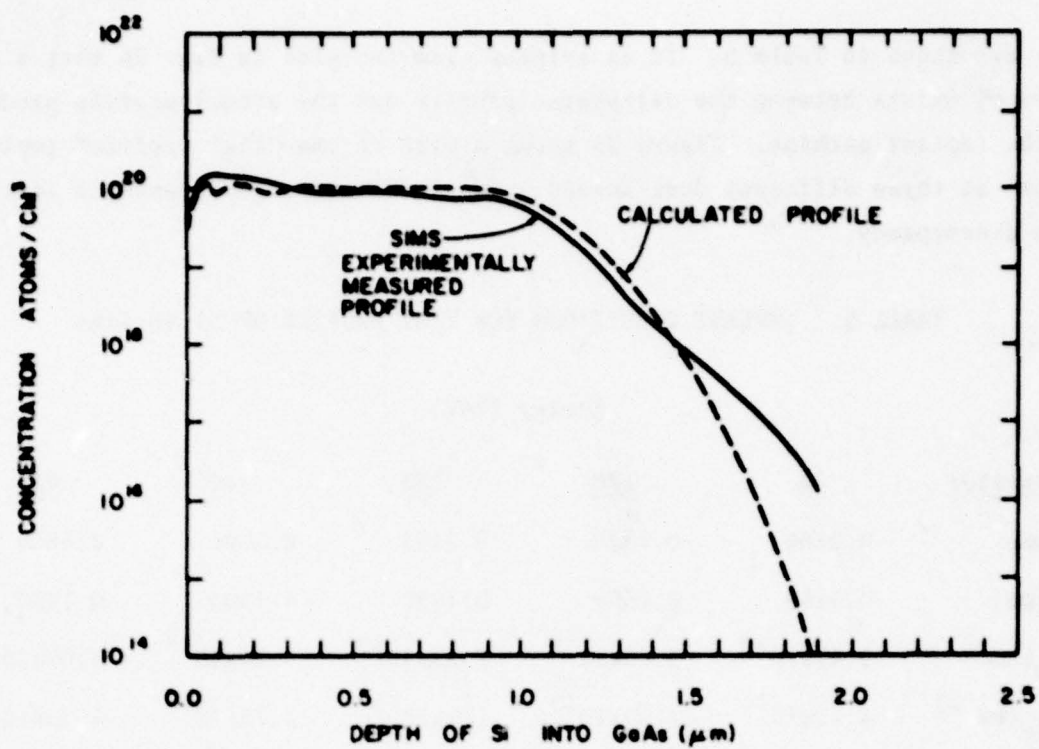


Figure 23. Comparison of calculated and actual SIMS profiles, log plot.

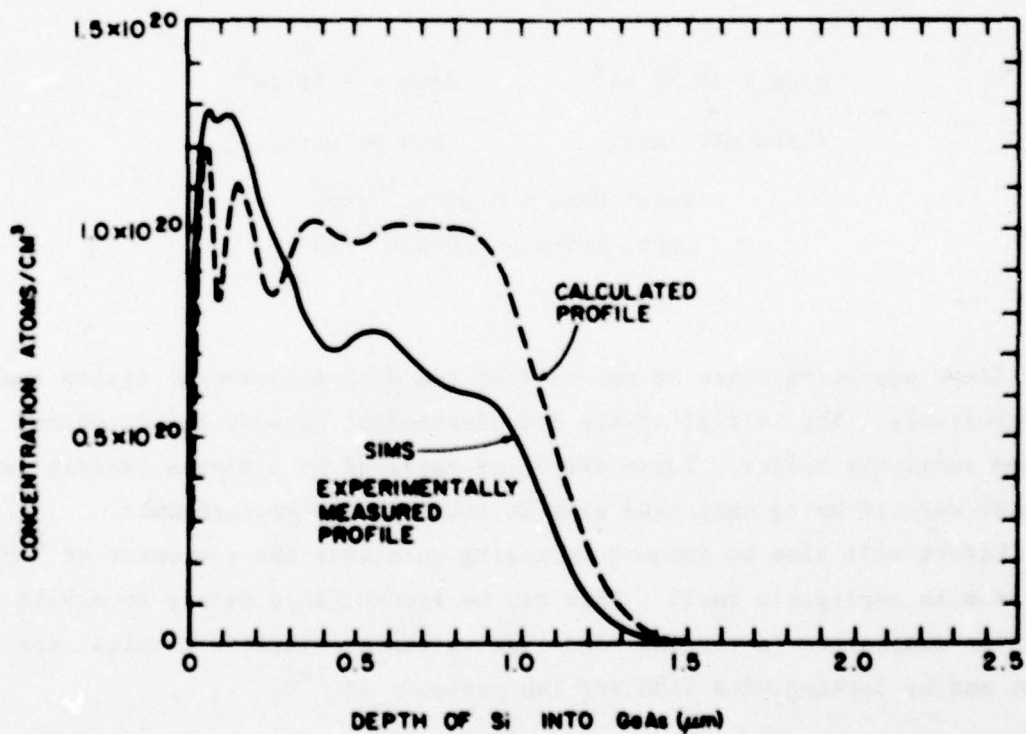


Figure 24. Comparison of calculated and actual SIMS profiles, linear plot.

data are shown in Table 5. It is evident from the plot in Fig. 24 that a discrepancy exists between the calculated profile and the actual profile produced by the implant machine. Figure 25 shows a plot of the "flat profile" implemented at three different dose levels. Sample H25 is a gross example of the dose discrepancy.

TABLE 5. IMPLANT CONDITIONS FOR FLAT PROFILE OF Si IN GaAs

Parameter	Energy (keV)				
	40	120	280	500	900
$R_p$ ( $\mu\text{m}$ )	0.0466	0.1375	0.3195	0.5500	0.8860
$\Delta R_p$ ( $\mu\text{m}$ )	0.0199	0.0600	0.1050	0.1500	0.1900
$N_{\text{max}}$ ( $\text{cm}^{-2}$ )	$9.47 \times 10^{19}$	$9.08 \times 10^{19}$	$7.23 \times 10^{19}$	$7.26 \times 10^{19}$	$9.09 \times 10^{19}$
$N_{\text{dose}}$ ( $\text{cm}^{-2}$ )	$4.70 \times 10^{14}$	$1.35 \times 10^{15}$	$1.9 \times 10^{15}$	$2.73 \times 10^{15}$	$4.33 \times 10^{15}$
Dose No.	303.6	872.0	1227	550.2	872.6
Scale	6E-6	6E-6	6E-6	6E-6	6E-6

$$\text{Area} = 24.29 \text{ cm}^2$$

(Lab. machine)

$$\text{Area} = 7.56 \text{ cm}^2$$

(FEC machine)

$$\text{Total Dose} = 1.08 \times 10^{16} / \text{cm}^2$$

$$\text{Conc. Level} = 1.00 \times 10^{20} / \text{cm}^3$$

Steps are being taken to ensure that the dose measurement system functions more reliably. The initial system had independent Faraday cup detectors and a heated substrate holder. These are being replaced by a single Faraday cup and greater care is being exercised with in situ leakage measurements.

Effort will also be focused on making sure that the component of  $^{28}\text{N}_2^+$  in the beam is negligibly small. This can be accomplished mainly by making sure that the components in the gas feed line in the accelerator terminal are leak-tight and by looking with SIMS for the presence of  $^{14}\text{N}$ .



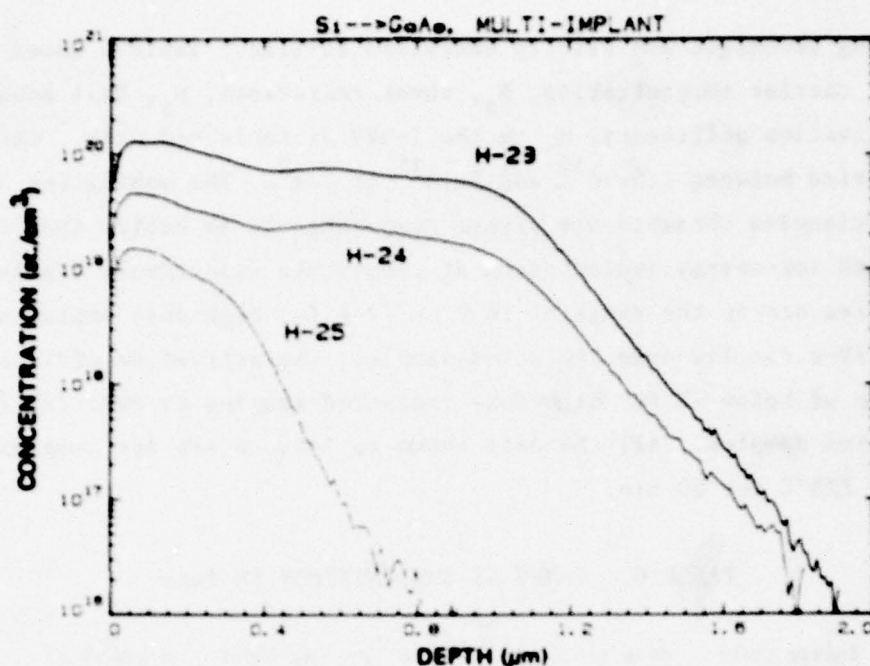


Figure 25. SIMS plots of the multiple-implant profiles formed using different dose levels.

In summary, the results of the high-energy implant experiments to date indicate that: (1) beams of  $^{11}\text{B}^+$  can be produced at energies up to 2 MeV, and (2) beams of  $^{28}\text{Si}^+$  can be produced at energies up to 1.2 MeV. SIMS analysis\* has proved to be a useful tool for analyzing the results of implant experiments, and curve-fitting technique, involving the calculation of the first four moments from the experimental data, can be used to approximate the measured profiles.

Further experiments are being planned to

- (1) investigate implants into amorphized substrates to study the amount of channeling occurring for  $7^\circ$  off-axis implants;
- (2) improve the accuracy of the dose measurement system; and
- (3) ensure that  $^{28}\text{N}^+$  components in the incident beam are negligible.

### 3. Mobility, Carrier Concentration, and Activation Efficiency

Following thermal annealing, the electrical characteristics of the high-energy implanted n-layers were evaluated by the van der Pauw measurement [22].

\*All SIMS measurements were made on unannealed samples.

The measuring technique was briefly described earlier. Table 6 shows the measured sheet carrier concentration,  $N_s$ , sheet resistance,  $\rho_s$ , Hall mobility,  $\mu$ , and the activation efficiency,  $\eta$ , on the 1-MeV Si-implanted GaAs. The implanted Si doses varied between  $1.5 \times 10^{13}$  and  $5 \times 10^{15}$  at./cm<sup>2</sup>. The mobilities and activation efficiencies obtained are either comparable to or better than those obtained with low-energy implantation at comparable dose levels (Table 2). The mobilities are in the range of 1690 cm<sup>2</sup>/V-s for high-dose implanted samples to 3980 cm<sup>2</sup>/V-s for low-dose implanted samples; the activation efficiencies are in the range of below 1% for high-dose implanted samples to over 73% for low-dose implanted samples. All the data shown in Table 6 are for samples capless-annealed at 825°C for 20 min.

TABLE 6. 1-MeV Si IMPLANTATION IN GaAs

Sample No.	Energy (keV)	Dose (at./cm <sup>2</sup> )	$N_s$ (cm <sup>-2</sup> )	$\rho_s$ ( $\Omega/\square$ )	$\mu$ (cm <sup>2</sup> /V-s)	$\eta$ (%)
M15	1000	$5.0 \times 10^{15}$	$3.67 \times 10^{13}$	85	2000	0.734
M16	1000	$1.5 \times 10^{15}$	$5.67 \times 10^{13}$	65	1690	3.78
M17	1000	$5.0 \times 10^{14}$	$7.33 \times 10^{13}$	49	1760	14.7
M18	1000	$1.5 \times 10^{14}$	$4.62 \times 10^{13}$	52	2620	30.8
M19	1000	$5.0 \times 10^{13}$	$2.7 \times 10^{13}$	70	3310	54.2
M20	1000	$1.5 \times 10^{13}$	$1.10 \times 10^{13}$	142	3980	73.5

The activation efficiency of heavily implanted samples increased at a higher annealing temperature. This result is shown in Table 7 where Si-implanted wafers were annealed at two different temperatures, 825 and 970°C. The two samples annealed at 970°C give rise to a higher activation efficiency. The annealing was done in a N<sub>2</sub> atmosphere with samples encapsulated with 2000-Å-thick reactively sputtered Si<sub>3</sub>N<sub>4</sub>. Mobility and sheet resistance data measured for samples implanted between 600 and 1200 keV at a dose level of  $3 \times 10^{15}$  at./cm<sup>2</sup> are summarized in Fig. 26.

Figure 27 shows the measured sheet carrier concentration as a function of Si dose for samples implanted at 200 keV and 1 MeV, respectively, and

TABLE 7. RESULTS OF Si-IMPLANTED WAFERS AT 825 AND 970°C

Sample No.	Energy (keV)	Dose (at./cm <sup>2</sup> )	Anneal Temp (°C)	N <sub>s</sub> (cm <sup>-2</sup> )	ρ <sub>s</sub> (Ω/□)	μ (cm <sup>2</sup> /V-s)	η (%)
M10	900	3.0x10 <sup>15</sup>	825	4.16x10 <sup>13</sup>	83.5	1800	1.39
			970	2.13x10 <sup>14</sup>	22.2	1320	7.10
M11	1000	3.1x10 <sup>15</sup>	825	3.73x10 <sup>13</sup>	92.7	1807	1.20
			970	1.47x10 <sup>14</sup>	27.4	1554	4.74

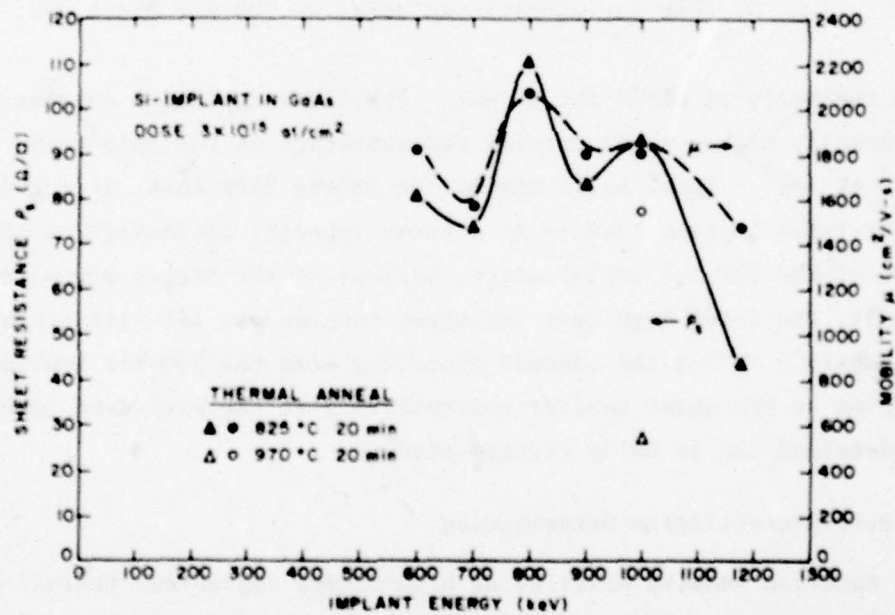


Figure 26. Mobility and sheet resistance measured after thermal annealing for samples implanted at different high-energy levels.



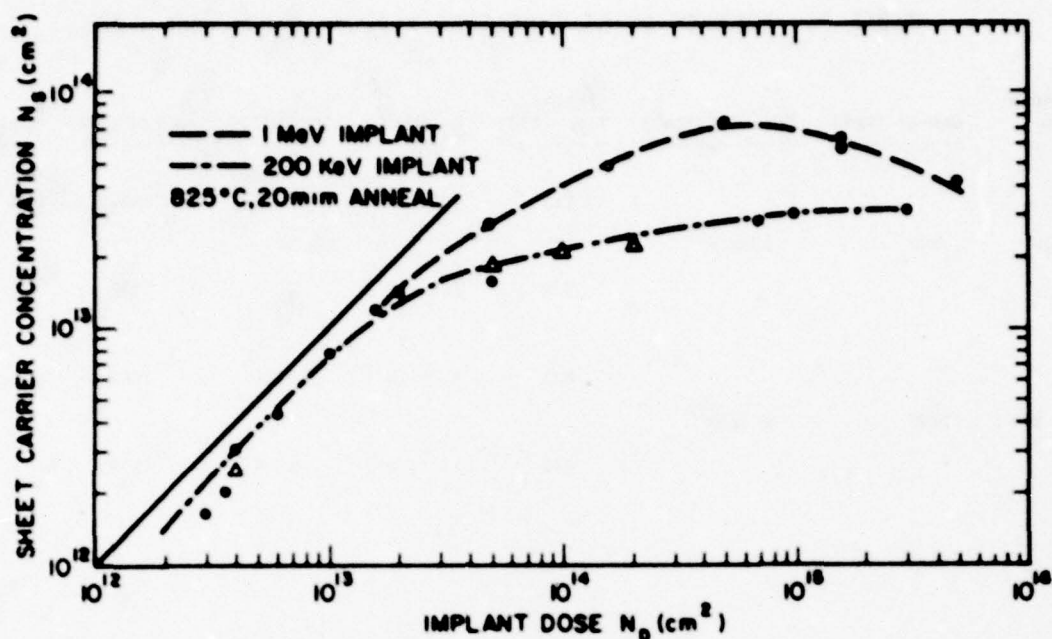


Figure 27. Measured sheet carrier concentration as a function of Si dose for samples implanted at 200 keV and 1 MeV.

annealed thermally at 825°C for 20 min. The 1-MeV implanted samples showed a substantially higher sheet carrier concentration in the dose range of  $5 \times 10^{13}$  to  $2 \times 10^{15}$  at./cm<sup>2</sup>. This result may be due to the fact that, at a given dose level, the 1-MeV implant results in a lower impurity concentration distribution than that of the 200-keV implantation, because of its higher straggle value. As a result, the 1-MeV high-dose implanted samples are less limited by the solid solubility during the thermal annealing than the 200-keV implant samples. The drooping in the sheet carrier concentration at the high-dose level is not fully understood and is being further studied.

#### 4. Carrier Concentration Distribution

The electron density profiles of high-energy implanted, thermal-annealed samples were evaluated using differential C-V measurement [26] in conjunction with controlled layer removal by chemical etching. Each controlled chemical etching step was between 500 and 1500  $\mu\text{m}$  depending on the electron densities of the layer being removed. Large etching steps were used for low-density regions ( $\leq 10^{17}/\text{cm}^3$ ). Schottky-barrier diodes were formed by evaporation of aluminum on to the surface following each chemical etching step, and depth profiles were measured on automatic C-V profile equipment.

Figures 28 to 31 show the electron concentration distribution of Si-implanted semi-insulating GaAs samples measured using this technique. Figures 28, 29, and 30 are for samples implanted at an energy level of 1 MeV, with fluences of  $1.5 \times 10^{14}$ ,  $5 \times 10^{13}$ , and  $1.5 \times 10^{13}$  at./cm<sup>2</sup>, respectively. The circular points shown in the figures are normalized data from SIMS measurement on a high-dose single-implanted (1 MeV) unannealed sample (Fig. 28). Figure 31 shows the profile of a multiple-implanted sample (H27) designed to produce a 1- $\mu$ m flat profile with a maximum impurity concentration of  $1 \times 10^{18}$  at./cm<sup>3</sup>. The implant parameters are therefore the same as those shown in Table 5, except all the fluences are two orders of magnitude lower. The samples were capless-annealed at 825°C for 20 min in an arsenic overpressure following implantation.

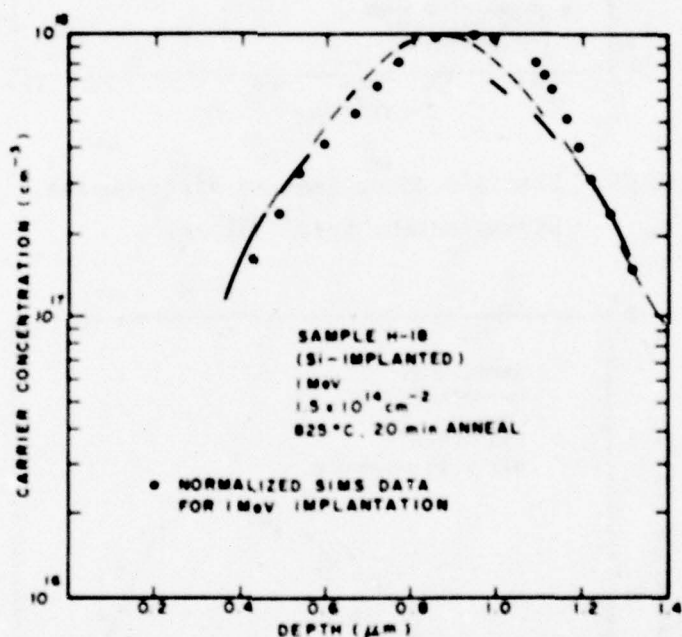


Figure 28. Electron concentration distribution, 1-MeV, Si-implanted,  $1.5 \times 10^{14}$  at./cm<sup>2</sup>.

The shape of the profiles determined from the differential C-V measurements show reasonable agreement with the SIMS measurements made on high-dose implanted unannealed samples (Figs. 28 and 30). The differences in range and standard deviation are approximately within 10% on the 1-MeV single energy implanted samples. The deviations between the multiple-implanted profiles determined by the SIMS and the C-V measurement are greater. This is expected because the C-V

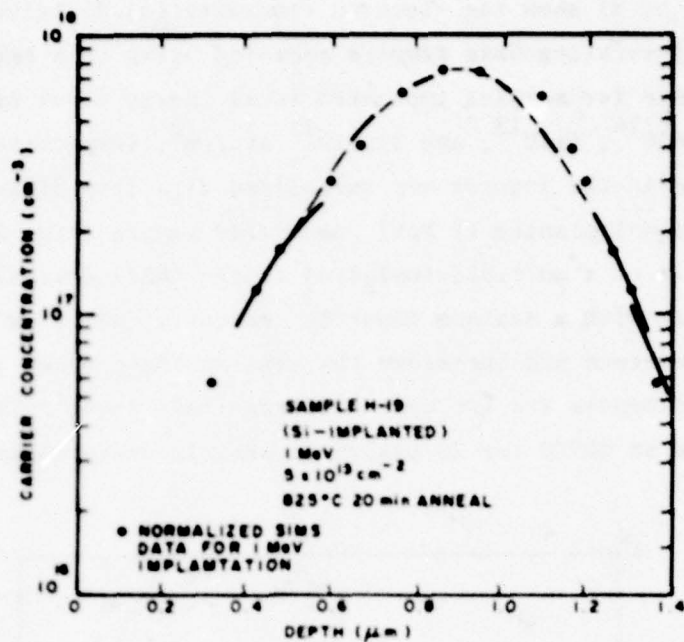


Figure 29. Electron concentration distribution, 1-MeV, Si-implanted,  $5 \times 10^{13} \text{ at./cm}^2$ .

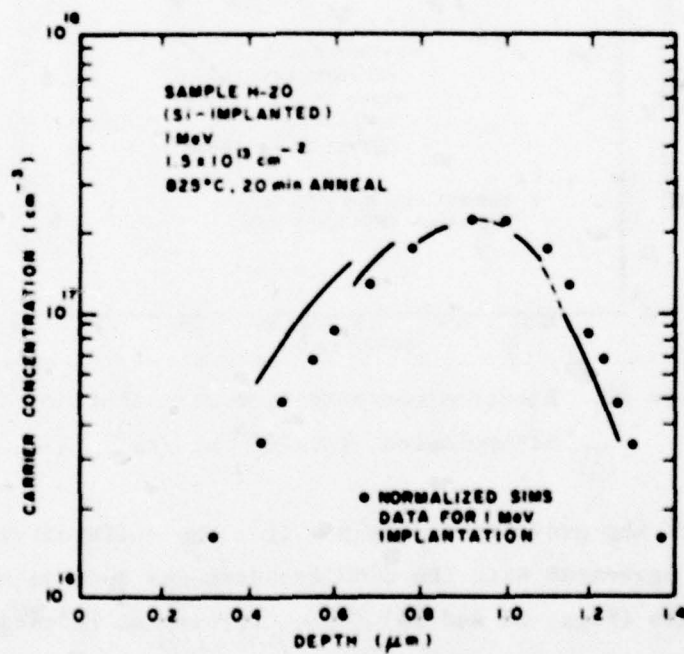


Figure 30. Electron concentration distribution, 1-MeV, Si-implanted,  $1.5 \times 10^{13} \text{ at./cm}^2$ .



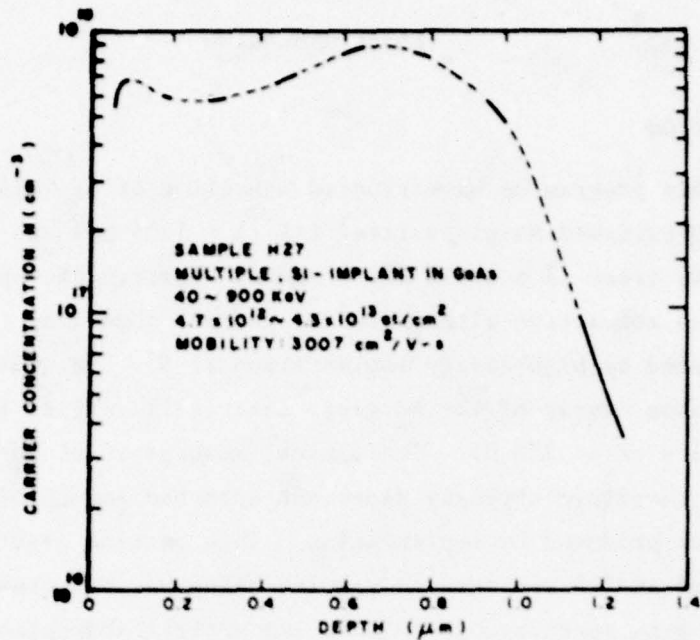


Figure 31. Carrier concentration of a multiple-implanted sample.

measurement determines the electrically active carrier concentration distribution, while the activation efficiency varies with amount of dose and energy. A better match can be obtained by including the dose-and-energy-dependent activation efficiency in the flat-profile design.

## SECTION IV

### LASER ANNEALING

#### A. INTRODUCTION

During this program we have studied annealing of Si-implanted GaAs with a high-power Q-switched Nd:glass laser [4] ( $\lambda = 1.06 \mu\text{m}$ ) and with a high-power Q-switched ruby laser ( $\lambda = 0.694 \mu\text{m}$ ). Recent research has shown that laser annealing is an attractive alternative to thermal annealing for removing lattice disorders created by high-energy implantation [1-5]. In contrast to the ruby laser, the photon energy of the Nd:glass laser (1.17 eV) is less than the band-gap of GaAs (1.4 eV at 300 K). The optical absorption at the Nd:glass laser wavelength is therefore strongly dependent upon the amount of impurities and lattice defects produced by implantation. This section describes studies made on as-implanted and laser-annealed samples using van der Pauw measurements, secondary ion-mass spectroscopy (SIMS), and optical absorption measurements. The results are compared with those obtained using thermal annealing. Surface morphology of laser-annealed GaAs layer and ohmic contacts made onto laser-annealed GaAs have been studied. Forming ohmic contacts onto laser-annealed high-dose implanted GaAs surface without alloying has been demonstrated.

#### B. HIGH-POWER PULSED LASER SYSTEM

The laser system used is the Korad Model K-1500 gigawatt laser system\* (Fig. 32). This consists of the oscillator, the amplifier, and the Pockel cell unit for Q-switching the oscillator output. The oscillator ruby rod is 10.16x0.95 cm (4x3/8 in.) diameter and is wrapped around by a helical xenon flashlamp, which serves to optically pump the laser material and produce a population inversion of the chromium ions in the ruby when at least half the chromium ions are excited. Lasing occurs when the round-trip gain between parallel mirrors placed at opposite ends of the oscillator ruby rod is greater than unity. The Pockel cell Q-switch prevents threshold for lasing from being attained by effectively reducing the reflectivity of the rear cavity mirror to zero. This allows the ruby rod to achieve a maximum energy storage, which

\*Hadron, Inc., Korad Div., Santa Monica, CA.

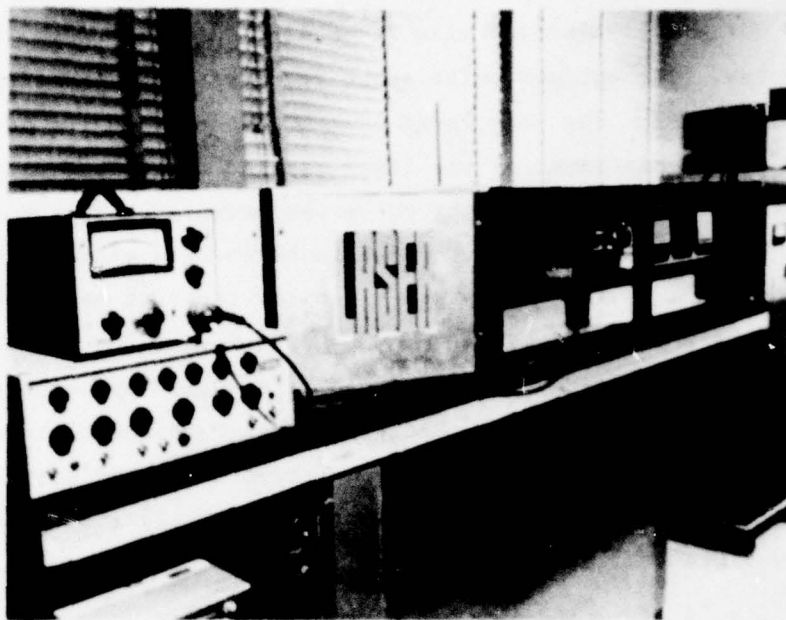


Figure 32. High-power pulsed laser system.

corresponds to a high value for the gain coefficient. The cell is then triggered to "insert" the cavity mirror, at which time a high cavity gain occurs. This results in a "giant pulse" with high power density and short pulse duration, typically 25 to 30 ns. This giant pulse is then further amplified by an amplifier stage. The amplifier ruby rod is 22.9x1.9 cm (9x3/4 in.) diameter and works by stimulated light emission triggered by the giant pulse from the oscillator stage and the Pockel cell. Amplification by a factor as high as 20X can be achieved. Maximum laser output power is 1 GW/pulse at 2 pulses/min.

At a given oscillator rod high voltage above the threshold value of 3.98 kV, the laser output pulse width is a function of two parameters, namely, Q-switch shutter delay and Pockel cell bias voltage. These two parameters are independent of each other so that they can be optimized separately. The laser output pulse width was measured with a photodiode and a Tektronix\* 7704 fast oscilloscope. The photodiode used was a silicon avalanche photodiode, type C30902E from RCA Electro Optics and Devices.\*\* The rise time was specified to be 0.4 ns which was adequate for this application. The Tektronix 7704

\*Tektronix Inc., Beaverton, OR.

\*\*RCA Electro Optics and Devices, Lancaster, PA.



oscilloscope was set up to operate in the triggered single sweep mode, and a camera with ultrafast Polaroid\* film (Type 410, ASA 10,000) was used to photograph the pulse. The optimum pulse shape recorded had a Gaussian distribution with a FWHM of 30 ns. The same laser system was modified for Nd:glass laser experiments with replacement of the laser rod and associated optical devices.

The energy of the laser output pulse was measured with a Korad K-J Calorimeter which gives a voltage output in microvolts proportional to the energy of the input pulse. The proportionality constant was 0.198 J/ $\mu$ V as specified and calibrated by Korad.

The laser output energy per pulse can be adjusted by varying the high voltage on the xenon lamps around the amplifier stage and/or around the oscillator stage. After firing the system for 5 or 6 times and reaching a thermal equilibrium in the laser rods, the output energy of the laser pulses is found to be reproducible to  $\pm 20\%$ .

#### C. PULSED Nd:GLASS LASER ANNEALING

Semi-insulating GaAs substrates of (100) orientation were implanted under high vacuum with  $^{28}\text{Si}^+$  at energies between 70 and 200 keV, and fluence between  $3 \times 10^{12}$  and  $3 \times 10^{15}$  at./cm<sup>2</sup>. The wafers were polished and chemically etched prior to implantation as previously described. Some wafers were polished on both sides to facilitate optical absorption studies. Following implantation, the 0.04-cm-thick wafer was cleaved to samples approximately between 0.5 and 2 cm<sup>2</sup> for laser-annealing experiments.

The Nd:glass laser was operated with an output energy density of between 0.2 and 2.5 J/cm<sup>2</sup> per pulse (25 ns). The corresponding power density lies between 8 and 200 MW/cm<sup>2</sup>. The diameter of the laser beam is 2 cm. The thermally annealed samples used for comparison were either annealed at 825°C for 20 min under an arsenic overpressure without encapsulation or annealed at temperatures up to 1000°C using samples encapsulated with a 2000-Å-thick sputtered Si<sub>3</sub>N<sub>4</sub> layer.

Figure 33 shows comparative results [4] of sheet carrier concentration density for Nd:glass laser and thermally annealed samples with implanted  $^{28}\text{Si}$  doses between  $3 \times 10^{12}$  and  $3 \times 10^{15}$  at./cm<sup>2</sup>. The energy density of each laser

\*Polaroid Corp., Cambridge, MA.

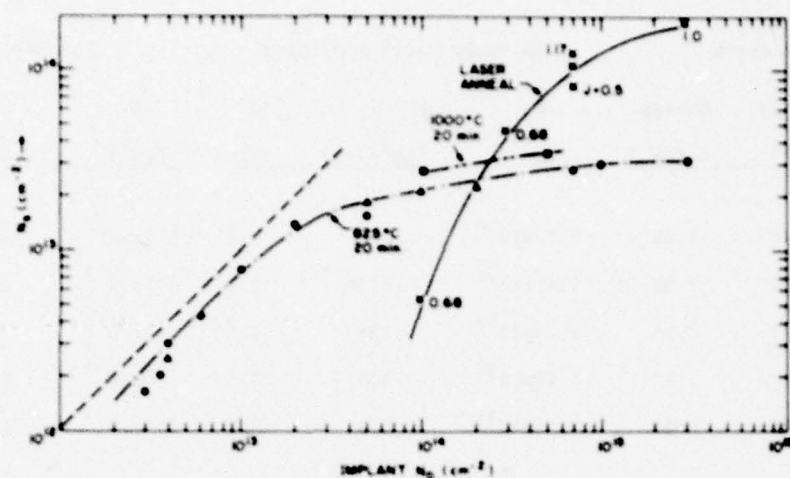


Figure 33. Comparison of thermal and laser annealing; 1.06- $\mu$ m, 25-ns single-pulse (Nd:glass) laser was used.

pulse used in the annealing is indicated by crosses in the figure; they vary between 0.5 and 1.17 J/cm<sup>2</sup>. All experiments were performed with single pulses. At the low energy density level, the implanted layers are only partially annealed. Comparison with Fig. 25 also shows that the electrical activation is greatly enhanced by laser annealing for samples implanted with doses higher than  $3 \times 10^{14}$  at./cm<sup>2</sup>. The sheet carrier concentration density  $N_s$  as determined by van der Pauw measurement is two-to-five times higher than that of samples thermally annealed at 825 or 1000°C for 20 min. The low electrical activation at a lower dose level for a given pulsed laser energy may be attributed to the reduction in enhanced optical absorption. This reduction is dependent on the amount of dose of the implantation as studied by the optical absorption measurements [4].

Table 8 lists some measured results on the mobility, the sheet carrier concentration, and the activation efficiency on Si-implanted GaAs samples annealed by a Nd:glass laser and by thermal anneal. The fluence listed in the table are greater than  $3 \times 10^{14}$  at./cm<sup>2</sup>. The laser-annealed samples showed higher activation efficiencies. The mobility for laser-annealed samples are comparatively lower. For example, mobilities for laser-annealed samples are 253 cm<sup>2</sup>/V-s at a sheet carrier concentration of  $1.91 \times 10^{14}$  at./cm<sup>2</sup>, and 529 cm<sup>2</sup>/V-s at  $1.25 \times 10^{14}$  at./cm<sup>2</sup>, compared with a mobility of 1392 cm<sup>2</sup>/V-s, at  $2.9 \times 10^{13}$  at./cm<sup>2</sup> and 1881 cm<sup>2</sup>/V-s at  $2.8 \times 10^{13}$  at./cm<sup>2</sup> for similar samples annealed thermally.

TABLE 8. COMPARISON OF THERMAL AND Nd:GLASS LASER ANNEALING DATA

Si Implantation			Nd:Glass Laser Annealing			Thermal Annealing		
Dose ( $\text{cm}^{-2}$ )	Energy (keV)	Energy ( $\text{J}/\text{cm}^2$ )	$N_s$ ( $\text{cm}^{-2}$ )	$\mu$ ( $\text{cm}^2/\text{V}\cdot\text{s}$ )	$\eta$ (%)	$N_s$ ( $\text{cm}^{-2}$ )	$\mu$ ( $\text{cm}^2/\text{V}\cdot\text{s}$ )	$\eta$ (%)
$3.0 \times 10^{15}$	70	1.00	$1.91 \times 10^{14}$	253	6.4	$5.1 \times 10^{13}$	1392	1.7
$3.0 \times 10^{15}$	200	2.25	$1.45 \times 10^{14}$	1017*	4.8	$3.3 \times 10^{13}$	1909	1.1
$1.0 \times 10^{15}$	70	0.34	$6.55 \times 10^{13}$	254	6.6	$3.2 \times 10^{13}$	1770	3.2
$5/2 \times 10^{14}$	200/70	1.17	$1.25 \times 10^{14}$	529	17.9	$2.8 \times 10^{13}$	1881	4.0
$3.0 \times 10^{14}$	200	0.68	$4.60 \times 10^{13}$	522	15.3	$3.0 \times 10^{13}$	1540	10.0

\*Laser plus thermal annealing,  $\rho_s = 42 \Omega/\square$ .

The optical absorption in the sample was measured by spectrophotometry. The transmission through the sample and the reflection from the sample were measured on a Cary spectrometer in the 7000- to 12000-Å wavelength range. The absorption at a given wavelength (e.g., 1.06  $\mu\text{m}$ ) is calculated by the expression:

$$A = 1 - T - R$$

where A, T, and R are, respectively, absorption, transmission, and reflection which are all absolute values and are expressed in percentages. The enhanced absorption due to implantation damage is equal to  $A - A_0$ , where  $A_0$  is the absorption through the unimplanted sample. At 1.06- $\mu\text{m}$  wavelength, the measured value of  $A_0$  was typically 0.1. The reflectance was measured with reference to an aluminum mirror, and the absolute value is obtained through calibration. At 1.06  $\mu\text{m}$ , the reflectance of aluminum on glass is 0.862.

Figure 34 shows the reflectance measured on an as-implanted wafer and on the same wafer irradiated with a Nd:glass laser pulse at an energy density of 0.34  $\text{J}/\text{cm}^2$ . Because of the enhanced absorption in the high-dose implanted layer, the reflection is affected only by the front (implanted) surface. Consequently, the reflectance forms a continuous line as it passes through the absorption edge as shown in Fig. 34a. In the case of the annealed sample,



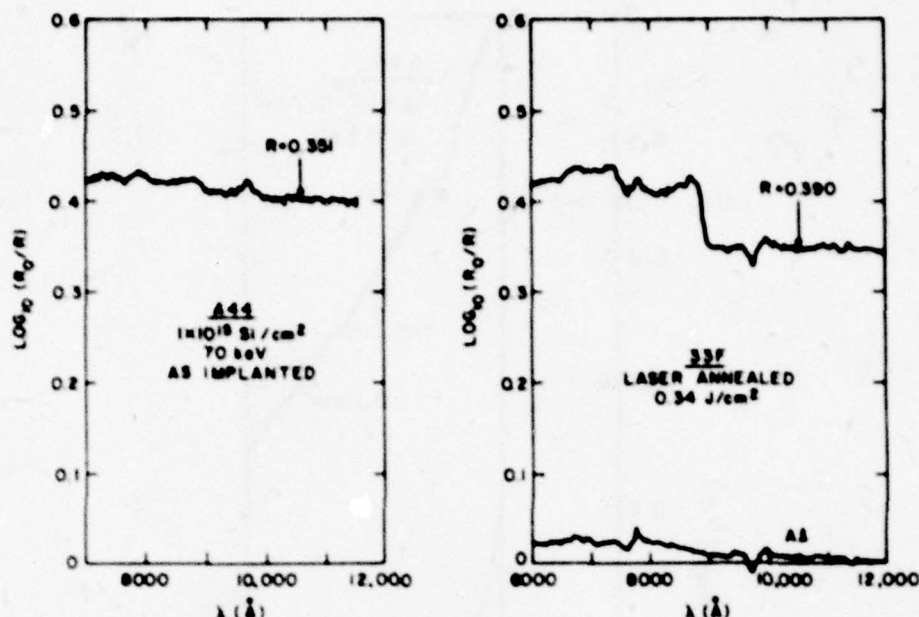


Figure 34. Reflectance measured on an as-implanted wafer (a) and after laser-annealing (b).

restored lattice order reduces the enhanced absorption in the implanted layer. As a result, the reflectance spectrum forms a step (Fig. 34b) as the optical wavelength passes through the band edge of GaAs, because the reflection is enhanced in the long wavelength range due to multiple reflection from the polished sample back surface. The multiple reflection dominates over the change in surface reflectivity which occurs as a result of implantation.

The transmittance through an ion-implanted sample before and after annealing is shown in Fig. 35. The gradual increase in absorption from the long-wavelength side toward the absorption edge in the as-implanted sample is a band-tailing effect produced by impurities [6]. The transmittance at 1.06- $\mu\text{m}$  wavelength changes from 0.170 for the as-implanted sample to 0.457 after laser annealing at 0.68 J/cm<sup>2</sup>. The enhanced absorption ( $A-A_0$ ) can be evaluated from the expression given in the previous section. Figure 36 shows the measured values of transmittance, reflectance, and enhanced absorption for as-implanted samples at different dose levels.

Optical absorption measurements show that the implantation enhanced absorption at a given wavelength (e.g., 1.06  $\mu\text{m}$ ) below the band edge increases with implant dose. This enhanced absorption is greatly reduced following annealing as a result of lattice re-ordering. Such optical measurement may thus be used

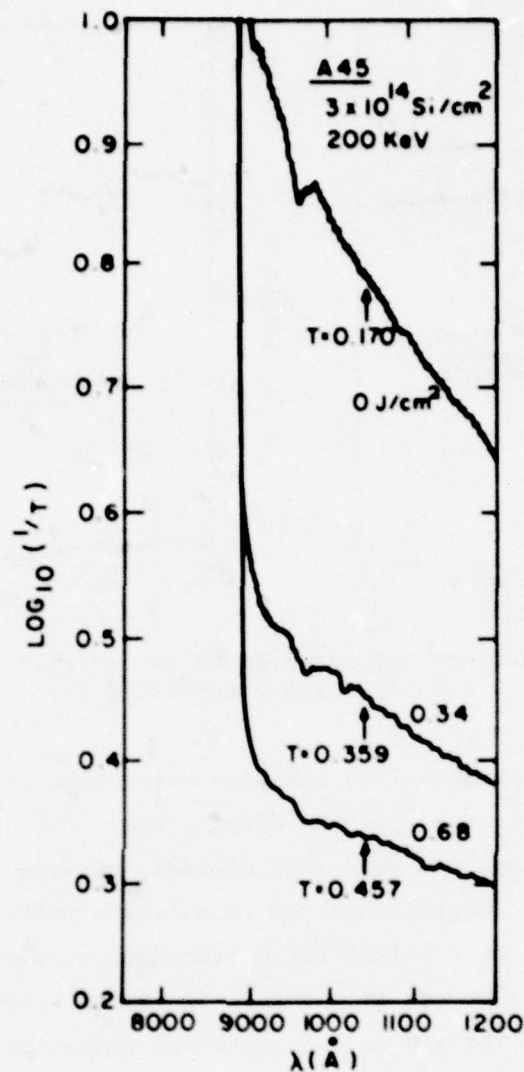


Figure 35. Optical transmission from Si-implanted GaAs sample annealed at different laser energy densities.

as a diagnostic technique for optimizing the required laser energy while maintaining good surface morphology.

#### D. PULSED RUBY-LASER ANNEALING

Laser-annealing experiments were also carried out using a ruby laser on Si-implanted (100)-orientated semi-insulating GaAs substrate. The wafers were implanted at 70, 100, and 200 keV, with doses ranging between  $1 \times 10^{14}$  and  $1 \times 10^{16}$  at./cm<sup>2</sup>. The Q-switched ruby laser was operated with an output energy

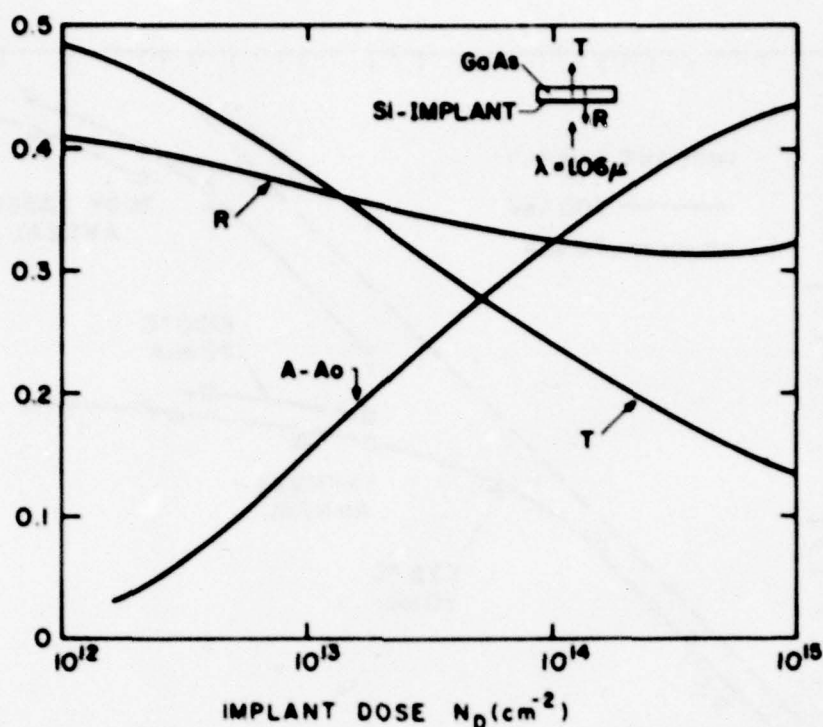


Figure 36. Measured values of transmittance (T), reflectance (R), and enhanced absorption (A-A $_0$ ) for different dose levels.

density of between 0.5 and 2.3 J/cm $^2$  per 30-ns pulse. The electrical characteristics of the laser-annealed samples were studied using the van der Pauw measurements.

Figure 37 shows results of sheet carrier concentration densities as a function of the implantation dose level for samples annealed by high-power pulsed ruby laser, and for samples annealed thermally. The thermal annealing was done at 825 and 1000°C for 20 min, and the energy used for implantation was at 200 keV, as described previously. The energy densities used for laser anneal shown in Fig. 37 were 1.7 and 2.3 J/cm $^2$ , which were higher than that plotted in Fig. 33. It is interesting to note that samples implanted at 200 keV show higher activation efficiencies than those implanted at 70 keV, at the high implant dose level. This may relate to the fact that the impurity density in the implanted layer is higher in the 70-keV implanted sample than in the 200-keV implanted sample because of the smaller straggle associated with the 70-keV implantation. Lower activation efficiencies were observed with increased fluence above  $5 \times 10^{14}$  at./cm $^2$  as shown in Fig. 37.

The sheet carrier concentration density of up to  $6.25 \times 10^{14}$  at./cm $^2$  with an activation efficiency of 20.8% was measured on high-dose implanted samples.



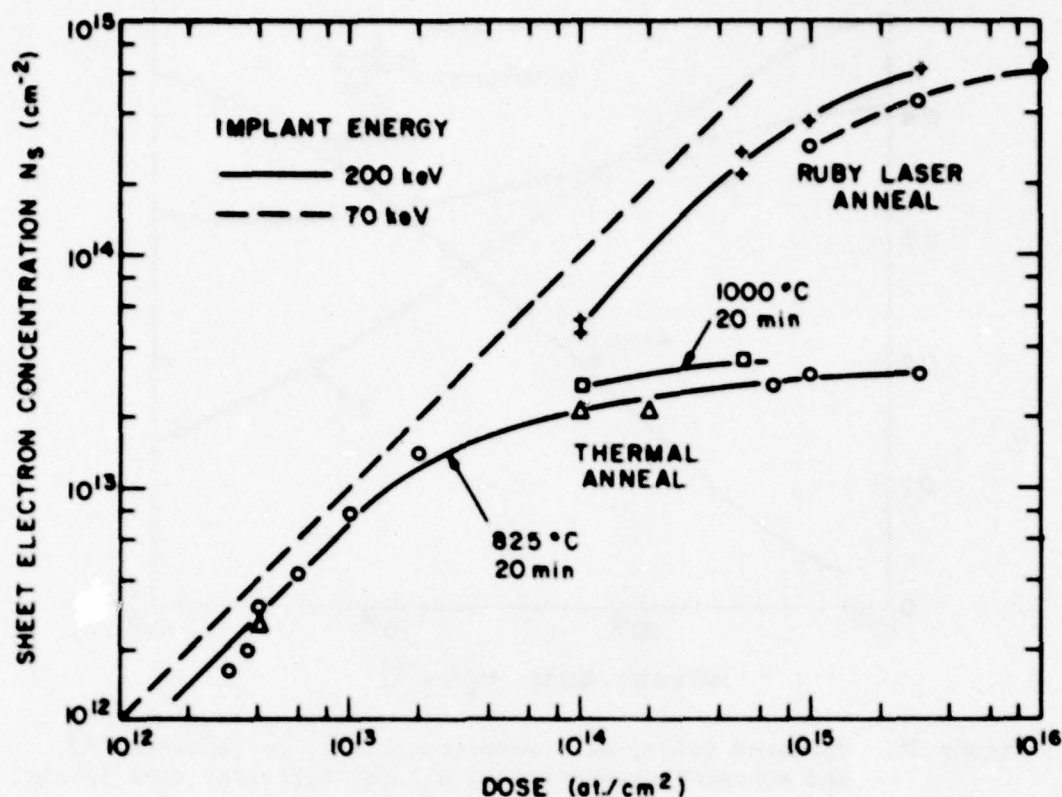


Figure 37. Sheet electron concentration as a function of dose for ruby-laser and thermal-annealed samples.

These results are more than an order of magnitude higher than that for similar samples annealed thermally. Figure 38 shows a plot of the mobility,  $\mu$ , the activation efficiency,  $\eta$ , and the sheet resistance,  $\rho_s$ , for 200-keV Si-implanted GaAs wafers implanted with three different fluences, and followed by a ruby-laser irradiation at  $2.3 \text{ J/cm}^2$ . Higher activation efficiencies (45 to 56%) and higher mobilities ( $930$  to  $1350 \text{ cm}^2/\text{V-s}$ ) were measured in wafers implanted at a dose level ranging from  $1 \times 10^{14}$  to  $5 \times 10^{14} \text{ at./cm}^2$ . The sheet resistances are lower and show little variations when the implant dose is higher than about  $5 \times 10^{14} \text{ at./cm}^2$ . The sheet resistances at the high-dose region shown in Fig. 38 are typically 4 to 5 times lower than similar thermally annealed wafers. The lowest sheet resistance obtained was  $20.8 \Omega/\square$ , which was measured on samples implanted at 70 keV with a dose of  $3 \times 10^{15} \text{ at./cm}^2$ , and annealed by ruby laser irradiation at  $2.3 \text{ J/cm}^2$ .

The electrical characteristics of ion-implanted laser-annealed samples depend on the implantation energy and fluence, and the energy density of the

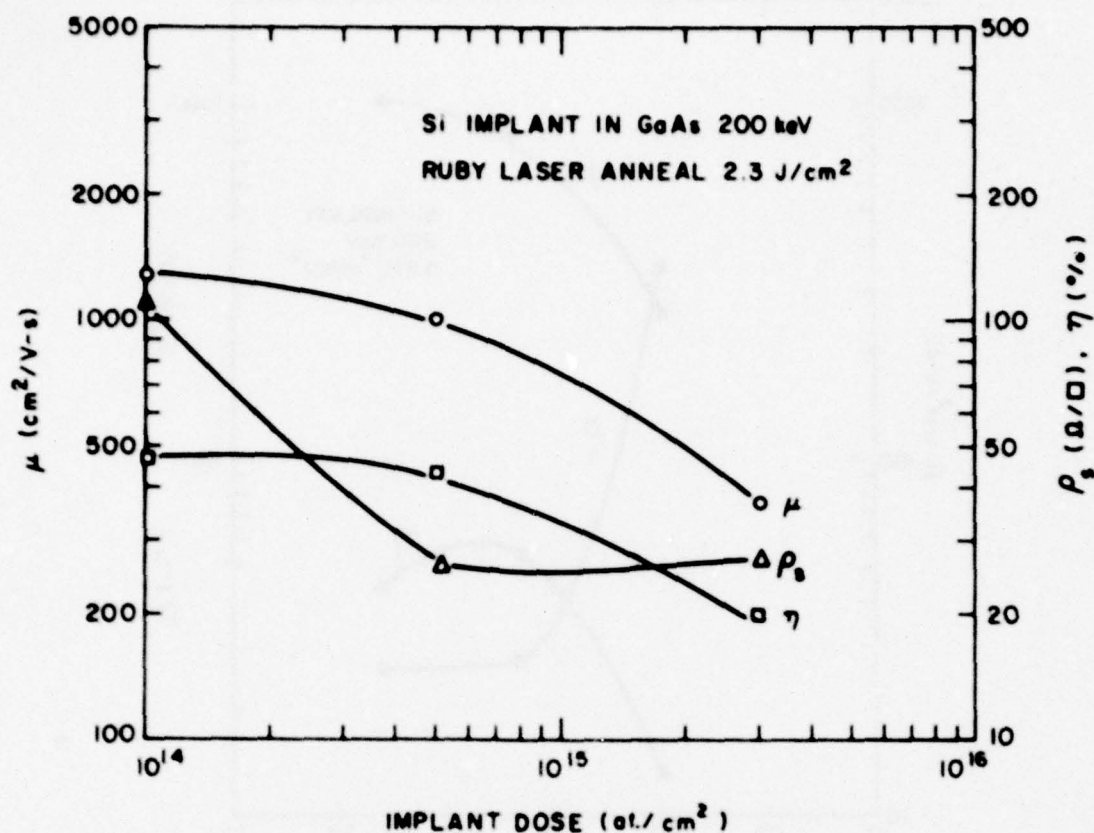


Figure 38. Mobility ( $\mu$ ), activation efficiency ( $\eta$ ), and sheet resistance ( $\rho_s$ ) as a function of dose.

laser irradiation on the sample surface. Figure 39 shows the measured mobility, the sheet resistance, and activation efficiency of a Si-implanted GaAs wafer irradiated by a ruby laser operated at different energy densities. The wafer was implanted at 200 keV with a fluence of  $5 \times 10^{14}$  at./cm².

The data points indicate that the mobility and activation efficiency are much higher for samples irradiated at a higher surface energy density (1.7 to 2.3 J/cm²) than that irradiated at a lower surface energy density (1 J/cm²). The sheet resistance drops substantially from 360 Ω/□ at 1 J/cm², to 27 Ω/□ at 1.7 to 2.3 J/cm². The sheet resistance starts to reach the low level at a laser energy density of about 1.5 J/cm², which may be considered as a threshold for full activation in this sample.

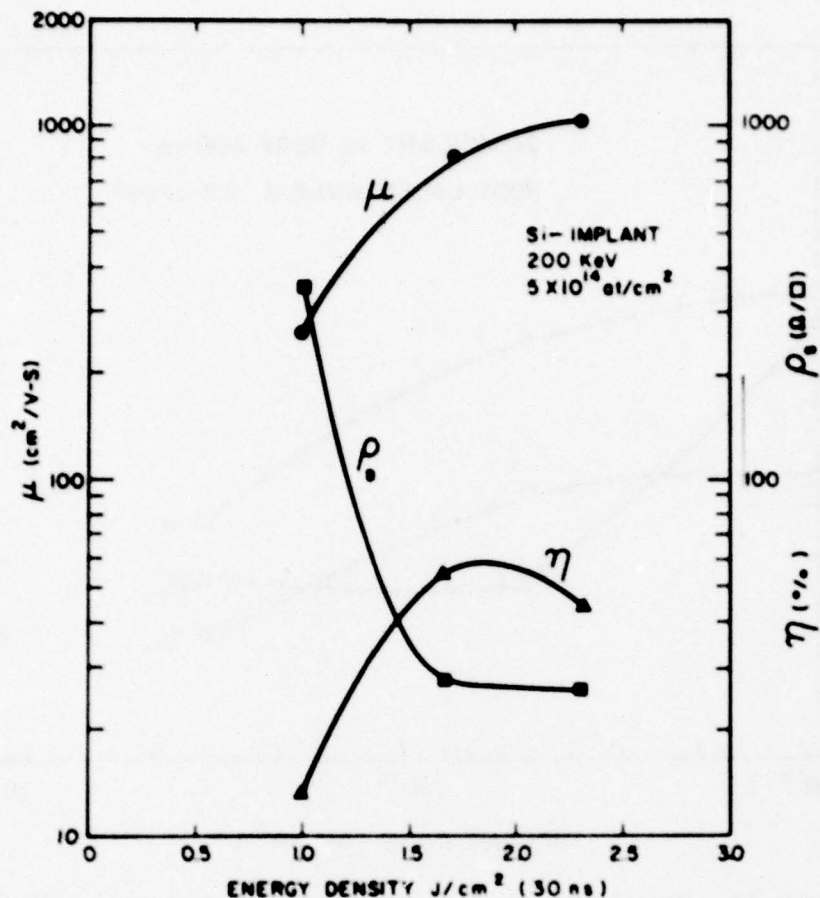


Figure 39. Mobility ( $\mu$ ), activation efficiency ( $\eta$ ), and sheet resistance ( $\rho_s$ ) as a function of energy density.

#### E. UNALLOYED OHMIC CONTACTS

The contact resistivity of ohmic contacts made onto GaAs has been reported to be inversely proportional to the carrier density of GaAs [37,38]. Contact resistivities of Au-Ge ohmic contacts on ion-implanted GaAs with different dose levels were studied using the TLM technique [39]. Since the laser-annealed heavily implanted GaAs layer shows a much higher activation than does the

37. W. D. Edward et al., "Specific Contact Resistance of Ohmic Contacts to GaAs," *Solid State Electron.* **15**, 388 (1972).
38. Y. Goldberg and B. V. Tsarenkov, "Dependence of the Resistance of Metal GaAs Ohmic Contacts on the Carrier Density," *Soviet Phys. Semicond.* **3**, 1447 (1970).
39. H. H. Berger, "Models for Contacts to Planar Device," *Solid State Electron.* **15**, 145 (1972). Also, *J. Electrochem. Soc.* **119**, 507 (1972).



thermally annealed layer, one expects a superior ohmic contact formed onto such a surface.

We investigated characteristics of contacts on the laser-annealed high-dose ( $1$  to  $3 \times 10^{15}$  at./cm<sup>2</sup>) Si-implanted SI GaAs wafers, and obtained encouraging results: ohmic contacts of low contact resistivity were formed by evaporation of Au-Ge/Ni/Au on to the laser-annealed surface without a subsequent alloying process. Normally an alloying step at 400 to 450°C is required in order to form the ohmic contact. Figure 40 shows the I-V characteristics between two unalloyed ohmic contacts. Forming a good ohmic contact on GaAs without alloying is obviously of great interest for the device and the integrated circuit fabrication.

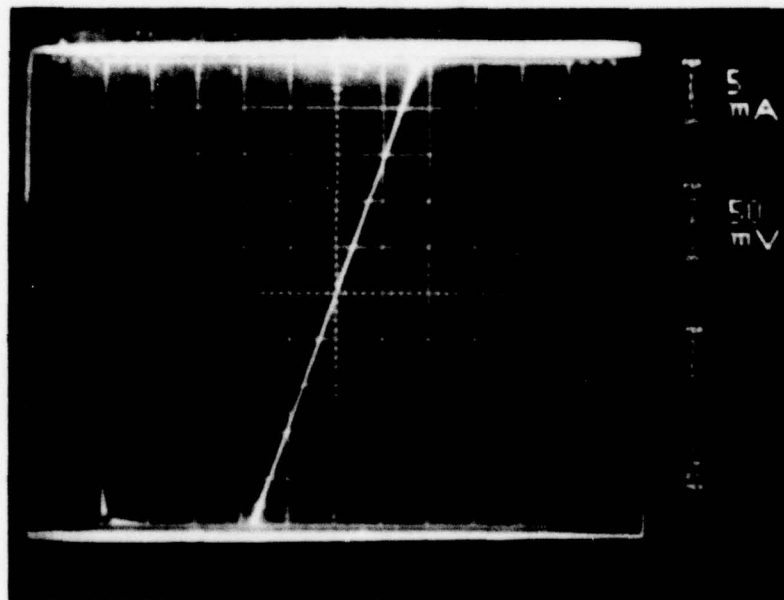


Figure 40. I-V characteristics between two unalloyed ohmic contacts.

The contact resistivity and the sheet resistance of the unalloyed contacts were measured using the TLM technique [39]. Identical rectangular shaped ohmic contacts with varying spacing between them were formed on the sample surface. The contact was made by evaporation of 900 Å of Au-Ge, 300 Å of Ni, and 1500 Å of Au. The patterns were formed by photolithography and lift-off. Mesas were etched for isolation of the test pattern from the remaining implanted layer. Because no alloying step was used following evaporation, no degradations occurred in the metal surface and in the conductivity of the metal.

Figure 41 shows the resistance between neighboring ohmic contacts measured as a function of spacing. From Fig. 41 the sheet resistance of the laser-annealed ion-implanted layer and the contact resistivity of the ohmic contact are deduced to be  $57.6 \Omega/\square$  and  $9.2 \times 10^{-6} \Omega\text{-cm}^2$ , respectively. The sheet resistance checked reasonably well with that from the van der Pauw measurement. The sheet resistance value was also checked by using a pattern with a wider spacing between two rectangular-shaped ohmic contacts. The large spacing increases the accuracy of  $\rho_s$ , hence, the slope  $dR/dx$ , and the accuracy of the measurement. The dimensions of the wider spacing between the contacts, and the width,  $W$ , of the contacts, are 148 and 240  $\mu\text{m}$ , respectively.

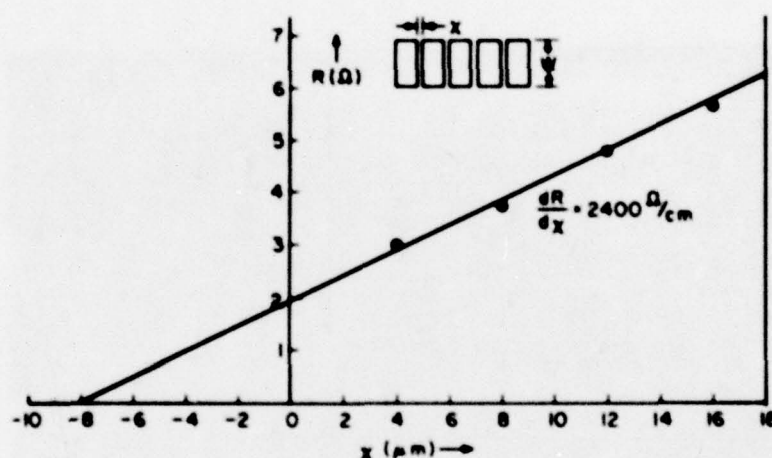


Figure 41. Resistance between neighboring ohmic contacts as a function of spacing.

#### F. SIMS MEASUREMENTS

Impurity distribution in as-implanted, thermal-annealed, Nd:glass laser-annealed, and ruby laser-annealed samples have been investigated with the SIMS technique. Depth profiles were obtained by bombarding the samples with 5 keV  $\text{Cs}^+$  ions [40,41] while detecting the implanted  $^{28}\text{Si}$  atoms as a molecular ion  $^{75}\text{As}^{28}\text{Si}^-$  at mass 103. Ultrahigh vacuum ( $4 \times 10^{-10}$  Torr) in the sample chamber during the analysis prevented interference from the molecular ion  $^{71}\text{Ga}^{16}\text{O}_2$  which is also at mass 103.

40. P. Williams, R. K. Lewis, C. A. Evans, and P. R. Hanley, "Evaluation of a Cesium Primary Ion Source on an Ion Microprobe Mass Spectrometer," *Anal. Chem.* **49**, 1399 (1977).
41. C. W. Magee, *J. Electrochem. Soc.* (in press).

The SIMS analyses show that the amount of impurity redistribution depends upon the energy and dose of implantation, and the energy density of the laser pulse used to anneal the sample. No redistribution occurred after irradiation with a low energy-density pulse, but a substantial impurity broadening was observed in high-dose implanted samples irradiated with a high energy-density pulse ( $\sim 2 \text{ J/cm}^2$ ). The broadening is believed to be associated with a diffusion in the liquid GaAs created by the high-energy laser pulse. An anomalous shoulder broadening effect was observed in the SIMS profile, after thermal annealing, in Si-implanted SI GaAs with high peak impurity concentration in the implanted layer; the anomalous broadening is believed to be associated with the damage-enhanced diffusion associated with the implantation.

Figure 42 shows the SIMS profile of a Si-implanted GaAs sample before and after thermal annealing ( $825^\circ\text{C}$ , 20 min). The sample was implanted at 200 keV with a dose of  $5 \times 10^{14} \text{ at./cm}^2$ . The peak impurity concentration was  $2.3 \times 10^{19} \text{ at./cm}^3$ . No impurity redistributions were observed after thermal annealing under these implantation conditions.

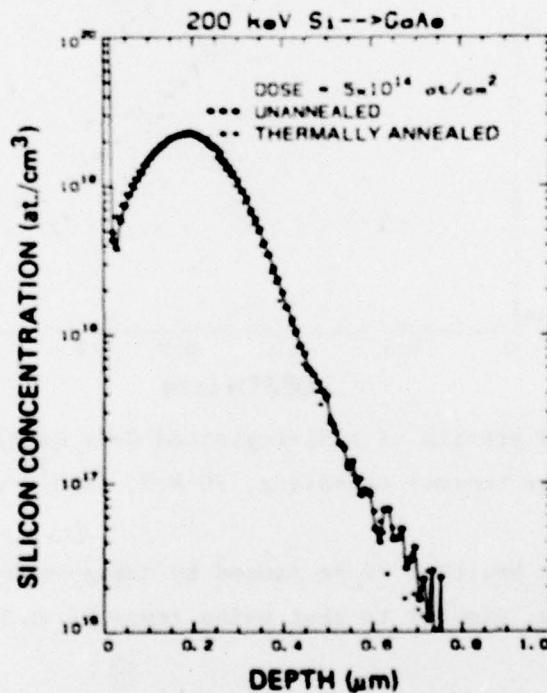


Figure 42. SIMS profile of a Si-implanted GaAs sample before and after thermal annealing, 200 keV,  $5 \times 10^{14} \text{ at./cm}^2$ .



Figure 43 shows the SIMS profile of a Si-implanted GaAs sample before and after thermal annealing under the same conditions. The sample was implanted at 70 keV with a dose of  $3 \times 10^{15}$  at./cm<sup>2</sup>. The peak impurity concentration was  $3.2 \times 10^{20}$  at./cm<sup>3</sup>. A shoulder broadening effect occurred at an impurity concentration of about  $3 \times 10^{18}$  at./cm<sup>3</sup>. The shoulder extends to a depth of 0.35  $\mu$ m.

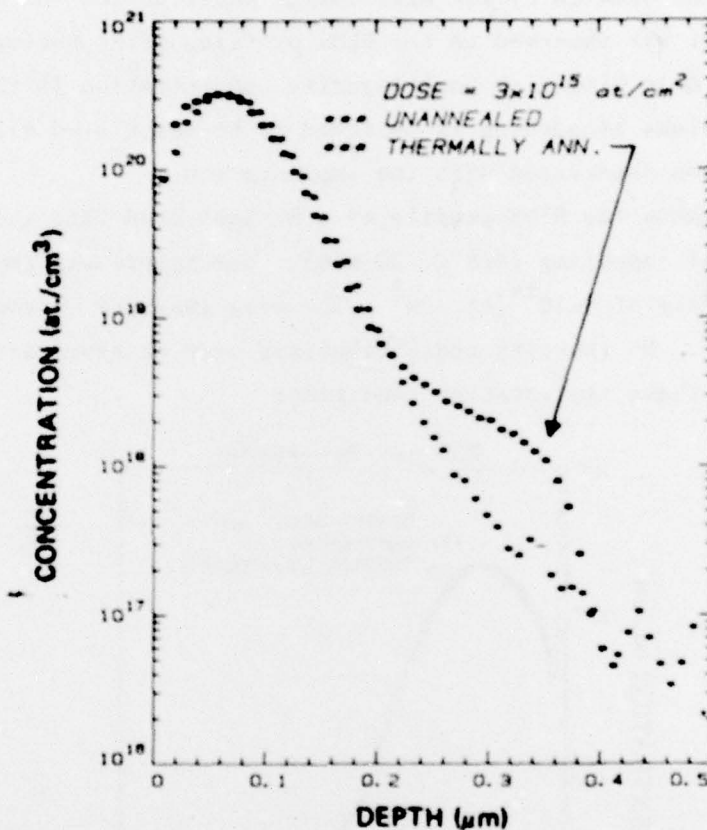


Figure 43. SIMS profile of a Si-implanted GaAs sample before and after thermal annealing, 70 keV,  $3 \times 10^{15}$  at./cm<sup>2</sup>.

These results are believed to be caused by damage-enhanced diffusion of unprecipitated silicon, similar to that being reported in Se-implanted GaAs [42].

42. A. Lidow, J. F. Gibbons, V. R. Deline, and C. A. Evans, Jr., "Solid Solubility of Selenium in GaAs as Measured by Secondary Ion Mass Spectrometry," *App. Phys. Lett.* **32**, 572 (1978).

Experiments here further demonstrated the dependence of anomalous broadening on the implantation conditions, which affect the degree of damage in the sample.

Figure 44 shows the SIMS profile [4] of a sample implanted at 70 keV with a dose of  $1 \times 10^{15}$  at./cm<sup>2</sup>, (peak impurity concentration  $\sim 10^{20}$  at./cm<sup>3</sup>) before and after irradiation with a low-energy density ( $0.3 \text{ J/cm}^2$ ) pulse (25  $\mu\text{s}$ ) from a Nd:glass laser. The profile shows no redistribution in impurity after irradiation with a single laser pulse up to about  $1 \text{ J/cm}^2$  in energy density.

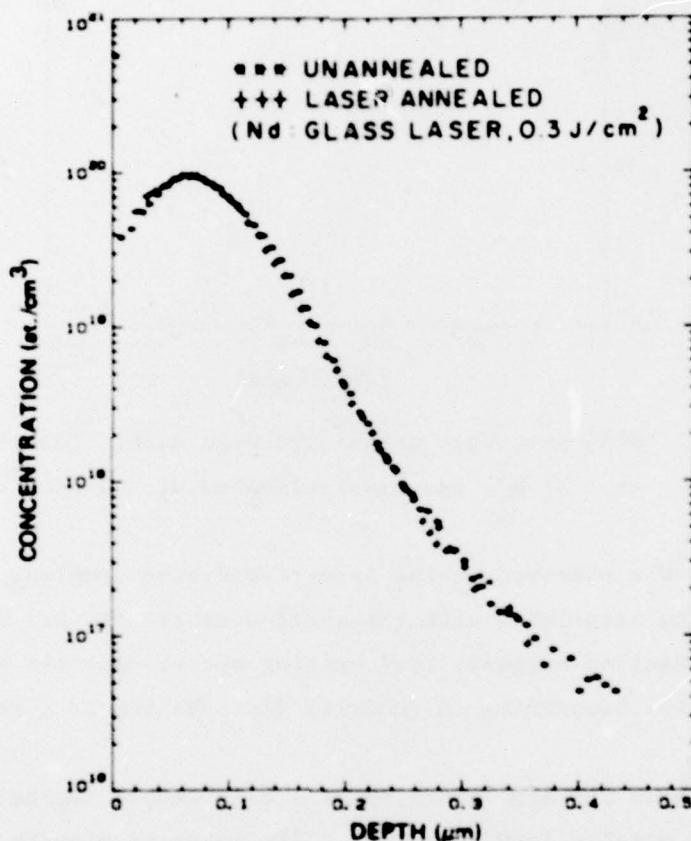


Figure 44. SIMS profile of a Si-implanted GaAs sample before and after laser annealing, 70 keV,  $1 \times 10^{15}$  at./cm<sup>2</sup>.

Figure 45 shows three SIMS profiles: one is the profile of a GaAs wafer as-implanted at 70 keV with a dose of  $3 \times 10^{15}$  at./cm<sup>2</sup>; the other two are samples from the same wafer after being irradiated with single ruby-laser pulses at energy densities of  $1.0$  and  $2.3 \text{ J/cm}^2$ , respectively. A redistribution in

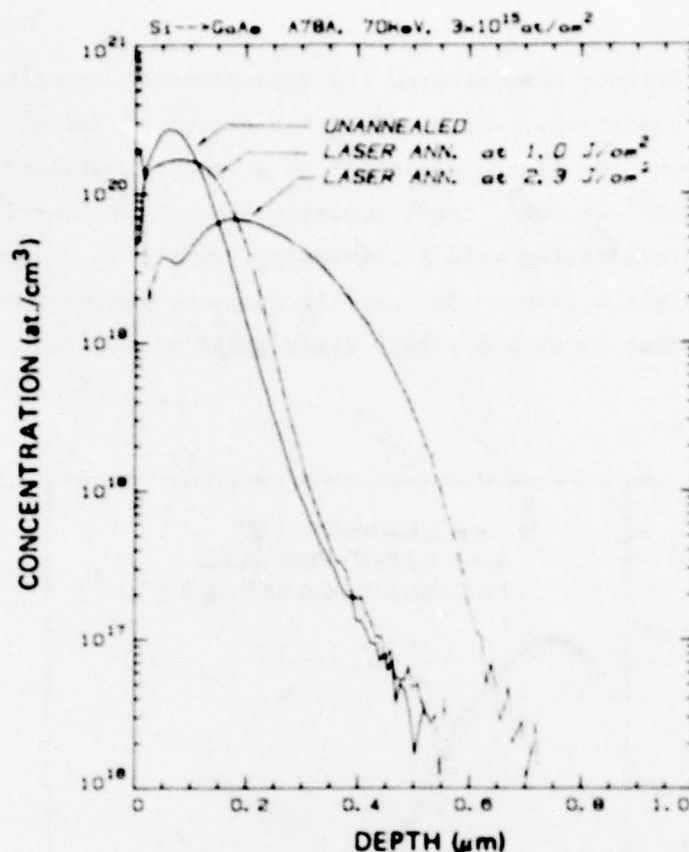


Figure 45. SIMS profiles: unannealed GaAs wafer; laser-annealed at  $1 \text{ J/cm}^2$ ; and laser-annealed at  $2.3 \text{ J/cm}^2$ .

impurity density was observed in the laser-irradiated samples. The impurity profile broadening associated with the short-duration (30 ns) high-energy laser pulse irradiation suggests that melting occurs near the surface region, and the substantial broadening in impurity distribution is a result of diffusion in liquid GaAs.

Figure 46 shows the SIMS profiles of a GaAs sample implanted at 70 keV with a very high dose of  $1 \times 10^{16} \text{ at./cm}^2$ . The impurity density of the as-implanted sample peaks at  $1 \times 10^{21} \text{ at./cm}^3$ . After thermal annealing (825°C, 20 min), the impurity profile does not vary except a shoulder broadening occurs at an impurity concentration of  $2 \times 10^{19} \text{ at./cm}^2$ . After irradiation with a  $2.3\text{-J/cm}^2$  ruby-laser pulse, the peak impurity concentration drops by an order of magnitude to about  $1 \times 10^{20} \text{ at./cm}^2$ , and the impurity penetrates to a depth of about  $0.8 \mu\text{m}$ . The deeper penetration depth associated with the higher impurity



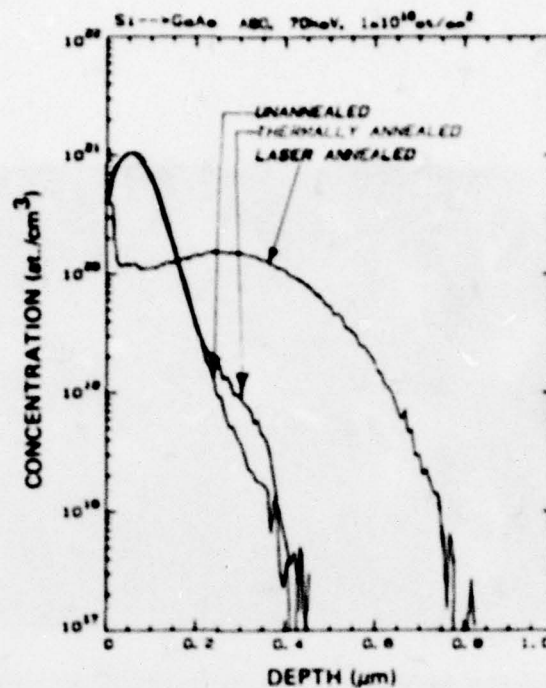
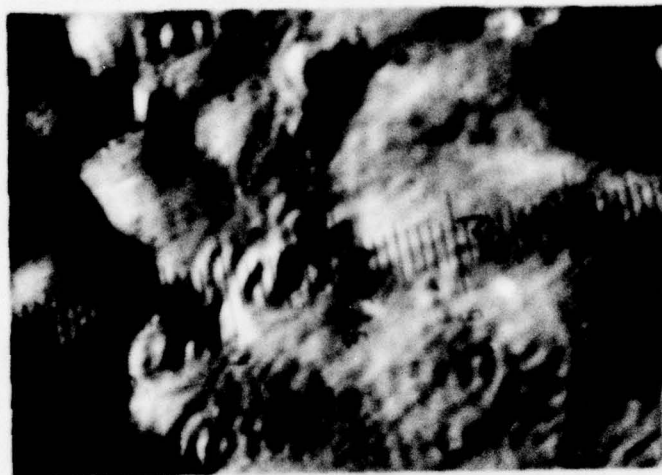


Figure 46. SIMS profiles: unannealed, thermal-annealed, laser-annealed samples.

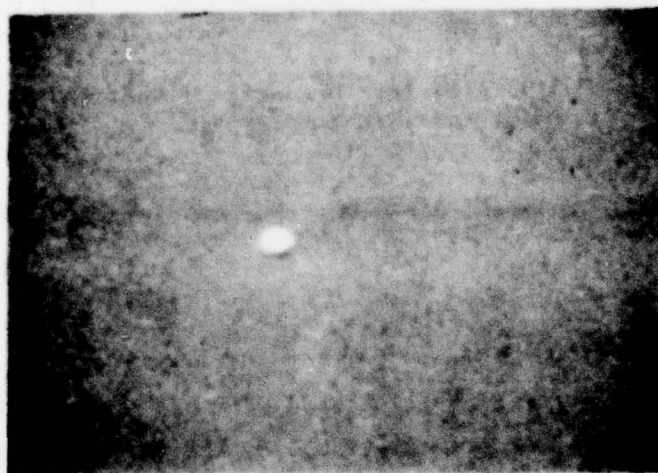
concentration further suggests the occurrence of diffusion in the melted GaAs surface layer.

#### G. SURFACE MORPHOLOGY STUDY

SEM photographs of samples irradiated with high energy-density pulse ( $2.3 \text{ J/cm}^2$ ) shows no structures detectable on the surface microscopically at 20K magnification, (Fig. 47b) although the sample surface visually appears wavy. A Nomarski interference contrast micrograph (Fig. 47a) shows an uneven rippled surface. These results suggest that melting and epitaxial regrowth are associated with annealing of GaAs by high energy-density laser pulse. Similar ripples [7] were observed on laser-annealed silicon surfaces, and it was suggested that the ripple formation occurs when the melting threshold is periodically exceeded. Examination of high-dose implanted GaAs samples irradiated with a laser pulse of  $1 \text{ J/cm}^2$  SEM reveals a fine structure (Fig. 48b) on the surface which does not appear on the as-implanted (Fig. 48a) sample. The various observed surface conditions created by different laser energy densities are being further investigated.



(a)



(b)

Figure 47. (a) Nomarski interference contrast. Ruby-laser anneal ( $2.3 \text{ J/cm}^2$ ) sample. (b) SEM of same sample at 20K magnification.



(a)



(b)

Figure 48. SEM photographs. (a) As-implanted sample at 20K magnification. (b) Ruby-laser-annealed sample at  $1\text{-J/cm}^2$  energy density (20K magnification).



## SECTION V

### SUMMARY AND CONCLUSIONS

This program was aimed at two major areas. High-energy implantation of donors into GaAs and the use of high-power lasers for annealing implanted GaAs layers were investigated. We have made significant progress in both areas. The progress made in these and related areas is summarized below.

- (a) We have investigated implantation of  $^{28}\text{Si}^+$  into SI GaAs up to an implant energy level of 1.2 MeV. A corresponding range of 1.1  $\mu\text{m}$  was measured by SIMS. The electrical activation and mobility following thermal annealing are comparable to or higher than (depending on implant parameters) that of thermally annealed low-energy (50 to 250 keV) implanted samples. A higher activation was observed in 1-MeV Si-implanted GaAs than in the 200-keV implants in the high dose region ( $10^{14}$  to  $10^{15}$  at./cm<sup>2</sup>). The electron density profiles measured on the 1-MeV implants showed a reasonable agreement with the normalized SIMS profile.
- (b) We have been studying the profiles and range statistics of  $^{28}\text{Si}$  implanted GaAs with implant energies of up to 1.2 MeV using SIMS analysis, and based on the information obtained, uniformly doped  $^{28}\text{Si}$  profiles  $\sim 1 \mu\text{m}$  deep have been produced in GaAs using multiple implants. After thermal annealing the measured electron density distribution confirms the 1  $\mu\text{m}$  depth with an average electron density of  $\sim 5 \times 10^{17}$  at./cm<sup>3</sup>.
- (c) We have been investigating laser annealing of high-dose Si-implanted GaAs using high-power pulsed Nd:glass laser and ruby laser. Electrical activation of high-dose, low-energy implanted samples are many times higher in laser-annealed samples than for those thermally annealed. Ohmic contacts formed onto laser-annealed samples without alloying have been demonstrated.
- (d) Optical absorption has been studied in Si-implanted GaAs wafers irradiated with high-power Nd:glass laser pulses. Measurements show that the implant-enhanced absorption at a given infrared wavelength increases with implant dose. The enhanced absorption is greatly reduced following annealing as a result of lattice reordering.

- (e) Impurity distribution in as-implanted, thermal-annealed, and laser-annealed samples have been investigated by SIMS analysis. The amount of impurity redistribution depends upon the energy and dose of implantation, and the energy density of the laser pulse used to anneal the sample. A substantial impurity broadening was observed in the high-dose implanted samples irradiated with a high energy-density ( $\sim 2 \text{ J/cm}^2$ ) pulse. The broadening is believed to be associated with a diffusion in the liquid GaAs created by the high-energy laser pulse. An uneven ripple observed on such a surface using a Normarski interference contract micrograph indicated the occurrence of melting at the sample surface.

An anomalous "shoulder broadening" effect was observed in the SIMS profile after thermal annealing in Si-implanted SI GaAs with a high peak impurity concentration in the implanted layer; the anomalous broadening is believed to be associated with the damage-enhanced diffusion associated with the heavy implantation.

- (f) Investigation of  $^{28}\text{Si}^+$  and  $^{32}\text{S}^+$  implants in GaAs at the low implant energy ( $< 300 \text{ keV}$ ) shows that the carrier concentrations are limited at the high dose to about  $3 \times 10^{18}/\text{cm}^3$  following the  $825^\circ\text{C}$ , 20 min thermal anneal, and limited at the low dose to about  $5 \times 10^{16}/\text{cm}^3$ . A "cutoff" fluence of about  $2 \times 10^{12} \text{ at./cm}^2$ , at 200-keV implant was observed in most GaAs substrates used for implant. The diffusion coefficient at the annealing temperature was 2 to  $5 \times 10^{-14} \text{ cm}^2/\text{s}$  for S in GaAs, and less than  $\sim 10^{-15} \text{ cm}^2/\text{s}$  for Si in GaAs. A capless thermal annealing process was used for ion-implanted GaAs wafers. The anneal is carried out under an arsenic overpressure which prevents decomposition of GaAs and results in good surface morphology.

## REFERENCES

1. E. I. Shtyrkov, I. B. Khaibullin, M. M. Zaripov, M. F. Galyatudinov, and R. M. Bayazitov, "Local Annealing of Implantation Doped Semiconductor Layers," *Sov. Phys. Semicond.* 9, 1309 (1976).
2. S. U. Compisano, I. Catalano, G. Foti, E. Rimini, F. Eisen, and M. A. Nicolet, "Laser Reordering of Implanted Amorphous Layers in GaAs," *Solid State Electron.* 21, 485 (1978).
3. R. T. Young, C. W. White, G. J. Clark, J. Narayan, W. H. Christie, M. Murakami, P. W. King, and S. D. Karner, "Laser Annealing of Boron-Implanted Silicon," *Appl. Phys. Lett.* 32, 139 (1978).
4. S. G. Liu, C. P. Wu, and C. W. Magee, "Annealing of Ion-Implanted GaAs with Nd:glass Laser," presented at the Symp. on Laser-Solid Interaction and Laser Processing held in Boston, MA, Nov. 28-Dec. 1, 1978. AIP Conference Proceedings No. 50, p. 603, New York, 1979.
5. B. J. Sealy, M. H. Badawi, S. S. Kular, and K. G. Stephens, "Electrical Properties of Laser-Annealed Donor-Implanted GaAs," *Electron. Lett.* 14, 720 (1978).
6. A. Gat and J. F. Gibbons, "A Laser-Scanning Apparatus for Annealing of Ion-Implantation Damage in Semiconductors," *Appl. Phys. Lett.* 32, 142 (1978).
7. W. L. Brown, J. A. Gdovchenko, K. A. Jackson, L. C. Kimerling, H. J. Leamy, G. L. Miller, J. M. Poate, J. W. Rodgers, G. A. Rozgonyi, T. T. Sheng, T. N. C. Venkatesan, and G. K. Celler, "Laser-Annealing of Ion-Implanted Semiconductors," *Proc. on Rapid Solidification Proc. - Principles and Technologies*, Reston, VA, Nov. 1977.
8. R. Tsu, J. E. Baglin, G. J. Lasher, and J. C. Tsang, "Laser-Induced Damage and Recrystallization of Ion-Implanted GaAs by Frequency-Doubled Nd:Yag Laser," AIP Conference Proceedings No. 50, p. 623, 1979 (c.f. Ref. 4).
9. F. H. Eisen et al., "Sulfur, Selenium, and Tellurium Implantation in GaAs," *Inst. Phys. Conf. Series No. 28*, p. 64, 1976.
10. R. K. Surridge and B. J. Sealy, "A Comparison of Sn-, Ge-, Se- and Te-ion-implanted GaAs," *J. Phys. D.* 10, 911 (1977).
11. J. K. Kung, R. M. Melton, and D. H. Lee, "GaAs FET'S with Silicon Implanted Channels," *Electron. Lett.* 13, 187 (1977).
12. A. G. Foyt, J. P. Donnelly, and W. T. Lindley, "Efficient Doping of GaAs by Se<sup>+</sup> Ion Implantation," *Appl. Phys. Lett.* 14, 372 (1969).
13. B. M. Welch, F. H. Eisen, and J. A. Higgins, "Gallium Arsenide Field-Effect-Transistors by Ion Implantation," *J. Appl. Phys.* 45, 3685 (1974).



14. W. K. Chu et al., Proc. 3rd Int. Conf. on Ion Implantation, (Plenum Press, New York, 1973).
15. R. D. Pashley and B. M. Welch, "Tellurium-Implanted  $N^+$  Layers in GaAs," Solid State Electron. 18, 977 (1975).
16. A. Lidow and J. F. Gibbons, "A Double-Layered Encapsulant for Annealing Ion-Implanted GaAs Up to 1100°C," Appl. Phys. Lett. 31, 158 (1977).
17. B. J. Sealy and R. K. Surridge, "A New Thin Film Encapsulant for Ion-Implanted GaAs," Thin Solid Films 26, L19 (1974).
18. A. A. Immoralica and F. H. Eisen, "Capless Annealing of Ion-Implanted GaAs," App. Phys. Lett. 29, 94 (1976).
19. D. H. Lee, R. M. Malbon, and J. M. Whelban, "Characteristics of Implanted N-type Profiles in GaAs Annealed in a Controlled Atmosphere," Ion-Implantation in Semiconductors, Ed. by F. Chernow et al. (Plenum Press, New York, 1976).
20. R. Zucca, "Electrical Compensation in Semi-Insulating GaAs," J. Appl. Phys. 48, 1987 (1977).
21. To be published.
22. L. J. van der Pauw, "A Method of Measuring Specific Resistivity and Hall Effect of Doses of Arbitrary Shape," Philips Res. Rep. 13, 1 (1958).
23. J. F. Gibbons et al., "Projected Range Statistics," (Halsted Press, A division of John Wiley and Sons, Inc. New York, 1975).
24. D. L. Rode and S. Knight, "Electron Mobility in GaAs," Phys. Rev. B3, 2534 (1971).
25. J. P. Donnelly, "Ion Implantation in GaAs," 1976 North American Symposium on GaAs and Related Compounds.
26. C. O. Thomas, D. Kahng, and R. C. Manz, "Impurity Distribution in Epitaxial Silicon Films," J. Electrochem. Soc. 109, 1055 (1962).
27. C. P. Wu, E. C. Douglas, and C. W. Mueller, "Limitations of the CV Technique for Ion-Implanted Profiles," IEEE Trans. on Electron. Devices 22, 319 (1975).
28. S. G. Liu, to be published.
29. A. B. Y. Young and G. L. Pearson, "Diffusion of Sulfur in GaP and GaAs," J. Phys. Chem. Solids 31, 517 (1970).
30. S. Asai and H. Kodera, "Electrical Properties of n-type Layers in GaAs prepared by Solid Sulfur Diffusion," Proc. of the 4th Int. Symp., Boulder, Colorado, p. 130, 1972.

31. P. L. Kendall, "Semiconductors and Semimetals," (Academic Press, New York, 1968), Vol. IV.
32. R. Baron, G. A. Shifrin, and O. J. Marsh, "Electrical Behavior of Group III and V Implanted Dopants in Silicon," J. Appl. Phys. 40, 3702 (1969).
33. J. W. Mayer, L. Eriksson, and J. A. Davies, "Ion Implantation in Semiconductors," (Academic Press, New York, 1970), p. 193.
34. M. G. Kendall and A. Stuart, The Advanced Theory of Statistics, (Charles Griffin, London, 1958), Vol. 1, p. 148.
35. W. P. Elderton, Frequency Curves and Correlation, (Cambridge University Press, 1953), 4th ed.
36. W. K. Hofker, Implantation of Boron in Silicon, Philips Research Supplements, 1975, No. 8.
37. W. D. Edward et al., "Specific Contact Resistance of Ohmic Contacts to GaAs," Solid State Electron. 15, 388 (1972).
38. Y. Goldberg and B. V. Tsarenkov, "Dependence of the Resistance of Metal GaAs Ohmic Contacts on the Carrier Density," Soviet Phys. Semicond. 3, 1447 (1970).
39. H. H. Berger, "Models for Contacts to Planar Device," Solid State Electron. 15, 145 (1972). Also, J. Electrochem. Soc. 119, 507 (1972).
40. P. Williams, R. K. Lewis, C. A. Evans, and P. R. Hanley, "Evaluation of a Cesium Primary Ion Source on an Ion Microprobe Mass Spectrometer," Anal. Chem. 49, 1399 (1977).
41. C. W. Magee, J. Electrochem. Soc. (in press).
42. A. Lidow, J. F. Gibbons, V. R. Deline, and C. A. Evans, Jr., "Solid Solubility of Selenium in GaAs as Measured by Secondary Ion Mass Spectrometry," App. Phys. Lett. 32, 572 (1978).

# DISTRIBUTION LIST

Contract N00014-78-C-0367

Code 427 Office of Naval Research Arlington, VA 22217	4	Mr. H. C. Nathanson Westinghouse Research and Development Center Beulah Road Pittsburgh, PA 15235	1
Naval Research Laboratory 4555 Overlook Avenue, S. W. Washington, DC 20375		Dr. Daniel Chen Rockwell International Science Center P. O. Box 1085 Thousand Oaks, CA 91360	1
Code 5211 5250	1		
Defense Documentation Center Building 5, Cameron Station Alexandria, VA 22314	12	Mr. G. J. Gilbert MSC 100 Schoolhouse Road Somerset, NJ 08873	1
Dr. Y. S. Park AFAL/DHR Building 450 Wright-Patterson AFB, OH 45433	1	Dr. C. Krumm Hughes Research Laboratory 3011 Malibu Canyon Road Malibu, CA 90265	1
ERADCOM DELET-M Fort Monmouth, NJ 07703	1	Mr. Lothar Wandinger ECOM/AMSEL/TL/IJ Fort Monmouth, NJ 07003	1
Texas Instruments M.S. 105/W. Wiseman P. O. Box 5936 Dallas, TX 75222	1	Dr. Harry Wieder Naval Ocean Systems Center Code 922 271 Catalina Blvd San Diego, CA 92152	1
Commanding Officer Office of Naval Research Branch Office 1030 East Green Street Pasadena, CA 91101	1	Dr. William Lindley MIT Lincoln Laboratory F124A P. O. Box 73 Lexington, MA 02173	1
Dr. R. M. Malbon/M.S. 1C Avantek, Inc. 3175 Bowers Avenue Santa Clara, CA 95051	1	Mr. Sven Roosild AFCRL/LQD Hanscom AFB, MA 01731	1
Dr. R. Bell, K 101 Varian Associates 611 Hansen Way Palo Alto, CA 94304	1	Commander U.S. Army Electronics Command V. Gelinovatch (DRSEL-TL-IC) Fort Monmouth, NJ 07703	1
Mr. R. Bierig Raytheon Company 28 Seyon Street Waltham, MA 02154	1		



Contract N00014-78-C-0367

RCA Microwave Technical Center Dr. F. Sterzer Princeton, NJ 08540	1	Commander Harry Diamond Laboratories Mr. Horst W. A. Gerlach 2800 Powder Mill Road Adelphia, MD 20783	1
Hewlett-Packard Corp. Dr. Robert Archer Page Mill Road Palo Alto, CA 94306	1	Advisory Group on Electron Devices 201 Varick Street, 9th floor New York, NY 10014	1
Watkins-Johnson Company E. J. Crescenzi, Jr./ K. Niclas 3333 Hillview Avenue Stanford Industrial Park Palo Alto, CA 94304	1	D. Claxton MS/1414 TRW Systems One Space Park Redondo Beach, CA 90278	1
Commandant Marine Corps Scientific Advisor (Code AX) Washington, D.C. 20380	1	Professor L. Eastman Phillips Hall Cornell University Ithaca, NY 14853	1
Communications Transistor Corp. Dr. W. Weisenberger 301 Industrial Way San Carlos, CA 94070	1	Dr. W. Wisseman, MS 118 Texas Instruments P. O. Box 225936 Dallas, TX 75265	1
Microwave Associates Northwest Industrial Park Drs. F. A. Brand/J. Salcom Burlington, MA 01803	1		
Commander, AFAL AFAL/DHM Mr. Richard L. Remski Wright-Patterson AFB, OH 45433	1		
Professor Walter Ku Phillips Hall Cornell University Ithaca, NY 14853	1		